ISTANBUL TECHNICAL UNIVERSITY ★ GRADUATE SCHOOL

DEEP UNFOLDING FOR CLUTTER REMOVAL IN GROUND PENETRATING RADAR

M.Sc. THESIS

Samet ÖZGÜL

Department of Communication Systems

Satellite Communication and Remote Sensing Programme

JUNE 2023

ISTANBUL TECHNICAL UNIVERSITY ★ GRADUATE SCHOOL

DEEP UNFOLDING FOR CLUTTER REMOVAL IN GROUND PENETRATING RADAR

M.Sc. THESIS

Samet ÖZGÜL
(705201014)

Department of Communication Systems

Satellite Communication and Remote Sensing Programme

Thesis Advisor: Prof. Dr. Işın ERER

JUNE 2023

İSTANBUL TEKNİK ÜNİVERSİTESİ ★ LİSANSÜSTÜ EĞİTİM ENSTİTÜSÜ

YERE NÜFUZ EDEN RADARDA KARGAŞA GİDERMEK İÇİN DERİN KATMAN AÇMA

YÜKSEK LİSANS TEZİ

Samet ÖZGÜL
(705201014)

İletişim Sistemleri Anabilim Dalı

Uydu Haberleşmesi ve Uzaktan Algılama Programı

Tez Danışmanı: Prof. Dr. Işın ERER

HAZİRAN 2023

Samet ÖZGÜL, a M.Sc. student of ITU Graduate School student ID 705201014, successfully defended the thesis entitled "DEEP UNFOLDING FOR CLUTTER REMOVAL IN GROUND PENETRATING RADAR", which he prepared after fulfilling the requirements specified in the associated legislations, before the jury whose signatures are below.

Thesis Advisor : **Prof. Dr. Işın ERER** ....
Istanbul Technical University

Jury Members : **Prof. Dr. Ender Mete EKŞİOĞLU** ....
Istanbul Technical University

Assoc. Prof. Nur Hüseyin KAPLAN ....
Erzurum Technical University

Date of Submission : 26 May 2023
Date of Defense : 16 June 2023

To my spouse and family,

FOREWORD

I would like to acknowledge and thank my supervisors, Prof. Dr. Işın Erer, for their guidance, assistance, and counsel during my MSc studies. I am also grateful to my family for their unwavering support. Finally, I want to express my appreciation to TÜBİTAK BİLGEM for their valuable contributions.

JUNE 2023

Samet ÖZGÜL
Software Engineer

TABLE OF CONTENTS

ABBREVIATIONS

GPR : Ground Penetrating Radar
PCA : Principal Component Analysis
ICA : Independent Component Analysis
SVD : Singular Value Decomposition
NMF : Non-negative matrix factorization
RPCA : Robust Principal Component Analysis
GoDec : Go-Decomposition
BRP : Bilateral random projections
RNMF : Robust Non-negative matrix factorization
CNN : Convolutional Neural Networks
AE : Autoencoders
SAR : Synthetic Aperture Radar
RAE : Robust AutoEncoder
YNR : Yere Nüfuz Eden Radar
TBA : Temel Bileşen Analizi
BBA : Bağımsız Bileşen Analizi
TDA : Tekil Değer Ayrışımı
NOMF : Negatif Olmayan Matris Faktarizasyonu
GTBA : Gürbüz Temel Bileşen Analizi
BRP : Bileteral Rastgle Projeksiyonlar
GNOMF : Gürbüz Negatif Olmayan Matris Faktarizasyonu
KEA : Konvolüsyonel Evrişimli Ağ
OK : Otomatik Kodlayıcılar
SAR : Sentetik Açıklıklı Radar
GOK : Gürbüz Otomatik Kodlayıcılar
AÇDÖ : Açığa Çıkaran Derin Öğrenme
LRPCA : Learned Robust Prinicipal Component Analysis
CORONA : Convolutional Robust Principal Component Analysis
GODEC-Net : Go-Decomposition Network
LRSD : Low-Rank and Sparse Decomposition
AltpPoj : Alternating Projections
ScaledGD : Scaled Gradient Descent
GD : Gradient Descent
RNN : Recurrent Neural Network
FRMMN : Feedforward-Recurrent-Mixed Meural Network
FNN : Feedforward neural network
ISTA : Iterative Shrinkage-Thresholding Algorithm
FISTA : Fast Iterative Shrinkage-Thresholding Algorithm
SVT : Singular Value Thresholding
PEC : Perfect Electric Conductor
PVC : Polyvinyl Chloride

LIST OF TABLES

LIST OF FIGURES

Page

DEEP UNFOLDING FOR CLUTTER REMOVAL IN GROUND PENETRATING RADAR

SUMMARY

Ground Penetrating Radar (GPR) is commonly used for identifying subterranean items, particularly plastic landmines that have a small amount of metal, cavities and pipelines [4] . Nevertheless, reflections emanating from subterranean targets are considerably impacted by the mess created by the direct connection between the antennas used for transmitting and receiving signals, reflections originating from the surface of the soil, and the scattering effect caused by objects other than mines, such as roots, gravel, or uneven terrain. The clutter is preventing to detect targets and decreases the performance of detection algorithms since it is dominating targets' reflections [5]. For this reason, the clutter removal of GPR images plays a critical role to detect clearly underground objects [6] [7].

For decades, lots of methods [7] are proposed for clutter removal from GPR images. The subspace decomposition techniques such as Principal Component Analysis (PCA), Independent Component Analysis (ICA), and Singular Value Decomposition (SVD) can be used to decompose [8] GPR images into distinct components corresponding to the clutter and the target based on their strength differences. Non-negative matrix factorization (NMF) [9] can be applied to GPR images to extract meaningful features and reduce the dimensionality of the data. Robust PCA (RPCA) decomposes a matrix to low-rank and sparse components. Due to high computational cost SVD operation in each iteration to solve non-convex minimizing operation that increases run-time. Several efforts have been made to accelerate the process of SVD operations in field studies suchs as Go-Decomposition (GoDec) which uses bilateral random projections (BRP) [10] to directly obtain the low-rank component. Also robust NMF (RNMF) [11] has been proposed, which includes a sparse component in the NMF decomposition. Deep learning methods are used in GPR imaging detection target and clutter removal tasks. The Robust AutoEncoder (RAE) is unsupervised deep learning method that can serve as a viable alternative to RPCA when it comes to decomposing a matrix into low-rank and sparse components. [12]. RAE employs the l_1-norm to break down a sparse matrix, much like RPCA does.

The following traditional methods have been proposed to reduce the high computational cost and working time: Learned Robust Principal Component Analysis (LRPCA), Convolutional Robust Principal Component Analysis (CORONA), and Go-Decomposition Network (GODEC). These proposed methods are referred to as Deep Unfolding Networks (DUN) [13] algorithms. In general, DUN algorithms convert each iteration of iterative methods into a deep learning layer in order to reduce the aforementioned computational cost and working time. LRPCA expands the concept of deep unfolding from a limited number of iterations to an infinite

number of iterations by utilizing a unique feedforward-recurrent-mixed neural network model. This approach allows LRPCA to improve the runtime performance during the testing phase compared to traditional methods, while also enabling the learnability of hyperparameters. On the other hand, CORONA is recognized for its fast algorithm, but its computational intensity is amplified due to the utilization of SVD in each iteration. However, a newly proposed method called GODEC-Net addresses this issue by employing BRP instead of SVD at each iteration. As a result, this modification significantly enhances the speed of regular operations for CORONA.

In this thesis study, a dataset is created using GPR images obtained from real-world conditions. The dataset is divided into two parts: training and testing. In order to train the DUN algorithms, the training dataset included not only raw data from GPR images but also separate images for target and clutter. To achieve this, the training dataset is initially decomposed into its components using RPCA. The proposed algorithms are compared visually and numerically with SVD, RPCA, RNMF, GoDec, and RAE. According to the obtained results, our proposed algorithms yielded similar results to other methods and, in some scenarios, are observed to perform better in clutter removal. LRPCA, although faster in terms of processing speed compared to CORONA and GODEC-Net, it has been demonstrated that CORONA and GODEC-Net perform better in clutter removal.

The aim of the thesis is to remove clutter in GPR images using deep unfolding networks, instead of computationally expensive and time-consuming algorithms. By doing so, it becomes more flexible to learn the iterative algorithm parameters that vary from one application to another using the proposed algorithms. This enables the realization of clutter removal in real-world applications.

YERE NÜFUZ EDEN RADARDA KARGAŞA GİDERMEK İÇİN DERİN KATMAN AÇMA

ÖZET

Yere Nüfuz Eden Radar (YNR), yer altı nesnelerini tespit etmek için yaygın olarak kullanılan bir teknolojidir [4]. YNR temel olarak verici anten, alıcı anten, görüntüleme ekranı ve merkezi kontrol bileşenlerinden oluşmaktadır. YNR üzerinde bulunan verici anten yer altına elektromanyetik sinyal gönderir böylelikle yer altındaki çeşitli nesnelerden ve hedeften yansıyan sinyaller alıcı anten ile toplanır. Alıcı antenlerden alınan veriler gerçek zamanlı olarak görüntüleme ekranına aktarılır ve YNR görüntüleri burada gösterilir. Aynı zamanda toplanan YNR verisi, daha sonra işlenmek üzere bilgisayar sabit diskine veya harici bir veri depolama ünitesine kaydedilebilir. YNR, arkeoloji, madencilik, mineral araştırmaları, şehir planlamalarında yer altı borularının tespiti ve kara mayınlarının tespiti gibi birçok uygulamada kullanılır.

Kara mayınları çoğu zaman çok az miktarda metal içeren veya sadece plastikten yapılmaktadır. Bu yüzden hedefin algılanması oldukça zordur, hatta metal dedektörlerinin plastik veya az metal malzemeden yapılmış mayınları tespit etmesi neredeyse mümkün değildir. Ancak, YNR bu tarz hedeflerin konumu, şekli, boyutları hakkında bilgi verebilmektedir. Bu yüzden YNR askeri çalışmalar için kritik öneme sahiptir.

Alıcı ve verici anten arasındaki kuplaj, hedefin yüzeye yakın olmasın, yeraltındaki bilinmeyen nesnelerden yansıyan sinyallerden, ağaç kökleri, ufak taşlar, toprak yapısı gibi birçok etken YNR sinyallerini etkileyerek kargaşa oluşmasına neden olur. Oluşan bu kargaşa (clutter) hedefin doğru şekilde algılanmasını güçleştirir veya yanlış algılanmasına sebep olur [5]. Kargaşa, YNR'nin en büyük sınırlaması olarak kabul edilir. Bu nedenle, YNR görüntülerinde kargaşanın kaldırılması, yer altı nesnelerini doğru bir şekilde tespit edebilmek oldukça önemlidir [6] [7].

Yıllar boyunca, YNR görüntülerinden kargaşanın giderilmesi için birçok yöntem [7] önerilmiştir. Başlıca yöntemler arasında Temel Bileşen Analizi (TBA), Bağımsız Bileşen Analizi (BBA) ve Tekil Değer Ayrışımı (TDA) gibi altuzay ayrışım teknikleri yer almaktadır. Bu teknikler, kargaşa ve hedef arasındaki sinyal güç farklarına dayanarak YNR görüntülerini farklı bileşenlere ayrıştırmak için kullanılabilir [8]. Ancak, optimal sonuçlara ulaşmak için altuzay teknikleri kargaşa altuzayının doğru bir şekilde belirlenmesini gerektirmektedir. Genellikle, kargaşa, hedeften yansıyan sinyalden daha güçlü olduğu için YNR görüntülerinde baskın bir bileşen olarak kabul edilirken, hedef ikinci bir bileşen olarak kabul edilir [14]. Bu nedenle birden fazla hedefin bulunduğu durumlarda, altuzay teknikleri kargaşa ve hedefi ayırmada başarılı olmayabilir çünkü iki hedefin sinyal güçleri birbirine yakındır. Negatif olmayan matris faktörizasyonu (NOMF) [10], anlamlı özelliklerin çıkarılması ve verilerin boyutunun

azaltılması için GPR görüntülerine uygulanabilir. NOMF'nin amacı, bir görüntünün matrisini yalnızca pozitif olmayan değerler içeren iki matrise ayrıştırmaktır. İlk matris, sütunlar tarafından temsil edilen temel vektörleri içerirken, ikinci matris, satırlar tarafından temsil edilen ağırlıkları içerir. Gürbüz Temel Bileşen Analizi (GTBA), bir matrisi düşük-rank ve seyrek bileşenlere ayrıştırır ve görüntü işleme, video arka plan çıkarma [15], tıbbi görüntülerde doku/kontrast ayrımı, gürültü giderme, değişim tespiti [16], YNR görüntülerinde kargaşanın giderilmesi [17] gibi birçok araştırma alanında kullanılmaktadır. GTBA, her iterasyonda TDA işlemi içerdiğinden yüksek hesaplama maliyetine sahiptir ve çalışma süresini yüksektir. TDA işlemlerinin sürecini hızlandırmak için çeşitli çalışmalar yapılmıştır. Bu amaçla, doğrudan düşük-rank bileşeni elde etmek için bilateral rasgele projeksiyonlar (BRP) [18] kullanan Go-Decompotision (GoDec) [18] gibi alternatif yöntemler geliştirilmiştir. Ayrıca, NOMF ayrışımına seyrek bir bileşen ekleyen yeni bir yaklaşım olan Gürbüz NOMF (GNOMF) [11] önerilmiştir.

Derin öğrenme yöntemleri son yıllarda YNR görüntülerindeki kargaşanın kaldırılması, hedefin sınıflandırması [19] ve gürültü azaltma gibi birçok uygulamada kullanılmıştır. YNR görüntülerindeki hedefleri tespit etmek veya sınıflandırmak için Konvolüsyonel Derin Ağ (KDA) temelli çeşitli teknikler geliştirilmiştir [20] [21]. Otomatik Kodlayıcılar (OK), YNR görüntülerinde anomalileri tespit etme [22], kargaşa bastırma [7] ve Sentetik Açıklıklı Radar (SAR) görüntülerini sınıflandırma [23] gibi gözetimsiz öğrenme görevlerinde sıkça kullanılan sinir ağlarıdır. Gürbüz Otomatik Kodlayıcılar (GOK), matrisi düşük-rank ve seyrek bileşenlere ayrıştırmak için GTBA yerine alternatif olarak kullanılabilir [12]. GOK, GTBA ile benzer şekilde seyrek bir matrisi l_1-normunu kullanarak ayrıştırır, ancak düşük-rank bileşeni yakalamak için otomatik kodlayıcının doğrusal olmayan temsil yeteneğini de kullanır. Bu, GOK'nin düzensiz kargaşa durumlarıyla başa çıkmada GTBA'dan daha etkili olmasını sağlar.

Yukarıdaki geleneksel yöntemlerin yüksek hesaplama maliyetini ve çalışma süresini azaltmak için, Öğrenen Gürbüz Temel Bileşen Analizi (ÖGTBA), Evrişimli Gürbüz Temel Bileşen Analizi (EGTBA) ve GODEC-Net yöntemleri önerilmiştir. Önerilen yöntemler Açığa Çıkaran Derin Öğrenme (AÇDÖ) algoritmaları olarak adlandırılır. Genel olarak AÇDÖ algoritmaları, iteratif yöntemlerin her bir iterasyonunu, bir derin öğrenme katmanına çevirir. Geleneksel yöntemlerin çok fazla iterasyon içermesi ve her bir yöntemin uygulamadan uygulamaya değişen parametresinin olması gerçek-dünya uygulamalarında kullanılmasını engellemektedir. AÇDÖ yöntemleri, genellikle manuel olarak seçilen ve her uygulama için değişen algoritma parametrelerini öğrenebilir hale getirir. Veriseti AÇDÖ yöntemleri ile eğitilmesiyle, her bir katmanda öğrenilen katsayılar ve parametreler daha sonra yeni veri için gerçek zamanlı uygulamalar için kullanılmasını mümkün kılmaktadır. [13].

AÇDÖ yöntemleri genellikle, iteratif algoritmaları belirli sayıda derin öğrenme katmanına açar ve bu modelin esnekliğini ve doğruluğunu kısıtlar. Ancak ÖGTBA, sabit katmanlı İleri Beslemeli Sinir Ağı (İBSA) modeline bir Yinelemeli Sinir Ağı (YSA) ekleyerek sonsuz katmanlı bir model olan İleri Beslemeli Yinelemeli Model ile Karışık Sinir Ağı (İBYKSA) elde eder. Elde edilen hibrit model ile hata, YSA sayesinde belirli bir koşul altında minimize edilir ve geleneksel kargaşa giderme yöntemlerinin performansına benzer sonuçlar elde edilir. EGTBA, Iterative

Shrinkage-Thresholding Algorithm (ISTA)'yı açarak evrişimli katmanlara dönüştürür. İteratif algoritmadaki matris çarpımları yerine evrişimli katmanların olması öğrenilen parametre sayısını düşürmektedir. EGTBA, ham YNR görüntüsündeki kargaşa ve hedefi ayırırken eğitim esnasında TDA kullanılır. TDA'nın kullanılması eğitim aşamasında algoritmanın çalışma süresini uzatmaktadır. Önerilen GODEC-Net algoritması bu sorunu çözmek TDA yerine BRP kullanarak, EGTBA'dan çalışma süresini 50% kısaltmaktadır.

Bu tezin amacı, çok fazla iterasyon gerektiren ve yüksek çalışma sürelerine sahip geleneksel metotlar yerine esnek, öğrenebilir ve hızlı AÇDÖ algoritmaları kullanarak gerçek ortamdan elde edilmiş YNR görüntülerinden kargaşayı gidermektir. Bu amaçla, gerçek ortam koşullarından elde ettiğimiz YNR görüntülerinden oluşan veriseti kullanılmıştır. Oluşturulan veriseti birçok farklı hedeften ve toprak tipinden elde edilmiş herbiri 50x50 piksel olan toplamda 898 adet YNR görüntüsü içermektedir. Oluşturulan verisetinin 75%'lik bölümü eğitim için kullanılırken 25%'lik kısmı da test için kullanılmıştır. Önerilen ÖGTBA, EGTBA ve GODEC-Net algoritmalarını eğitmek için, eğitim verisetine ham YNR görüntülerinin kargaşa ve hedef olarak ayrılmış görüntüleri de eklenmiştir. Eğitim verisetindeki görüntüleri kargaşa ve hedef olarak ayırmak için GTBA yöntemi kullanılmıştır. Eğitim aşaması tamamlandıktan sonra modellerin çıktıları kayıt edilmiş ve sonrasında bu çıktılar test verisetleri üzerinde denenmiştir. Sonuç olarak, gerçek ortamdan elde edilen yeni veriseti hem geleneksel hem de önerilen yöntemlerin kargaşa giderme performansları görsel ve nümerik olarak karşılaştırılmıştır. Önerilen AÇDÖ algoritmalarının geleneksel yöntemlere benzer sonuçlar verdiği hatta bazı senaryolarda geleneksel yöntemlerden daha iyi sonuçlar verdiği görülmüştür. Önerilen yöntemlerden ÖGTBA çalışma hızı bakımından EGTBA ve GODEC-Net'ten daha hızlı olmasına rağmen, EGTBA ve GODEC-Net kargaşayı bastırmada daha başarılı olduğu gözlemlenmiştir.

1. INTRODUCTION

1.1 Literature Review

Ground Penetrating Radar (GPR) is an electromagnetic geophysical method that is widely employed for efficiently detecting objects beneath the Earth's surface.. It finds extensive applications in various domains, including civil engineering, archaeology, mineral exploration, and military target detection. This non-destructive method offers remarkable accuracy and efficiency, making it a widely employed tool in these fields. In order to explore the subsurface, Ground Penetrating Radar (GPR) emits electromagnetic signals into the ground and collects the signals that are reflected back from various subterranean entities. Regrettably, the signals received by GPR are significantly influenced by direct reflections from the surface of the soil and reflections from non-target underground irregularities such as tree roots, rocks, and gravel, which are commonly referred to as clutter. Due to the clutter component often being stronger than the target component, the detection rates of underground objects decrease in many situations. Therefore, the elimination of the clutter from GPR images is crucial to enable precise identification of underground objects.

Subspace methods are widely utilized to remove clutter. These include the Singular Value Decomposition (SVD) and Principal Component Analysis (PCA), which decompose the matrix into various components [7]. However, in this case, when multiple targets exist, subspace methods do not perform well because that methods separate components as first, second, and remaining components respectively. Non-negative matrix factorization (NMF) [9] has been proposed as a method to separate a matrix of data into two matrices that contain only non-negative values. The first matrix consists of basis vectors, which are represented by its columns, and the second matrix consists of weights, which are represented by its rows. The initial matrix is made up of fundamental vectors, which are shown by the columns, while the second matrix is made up of coefficients, which are shown by the rows.

The Low-rank and Sparse Decomposition (LRSD) methods are used in various research fields, including image processing, video background subtraction, medical image analysis, denoising, and change detection. Robust Principal Component Analysis (RPCA) [24] is a technique that separates a matrix as low-rank and sparse components. The computational cost of RPCA is high due to the SVD operation that needs to be performed in each iteration to solve the non-convex minimizing operation, which leads to increased run-time. To address this issue, researchers have developed alternative methods, such as Go Decomposition (GoDec) [18] [10] and Robust NMF (RNMF) [11]. GoDec uses bilateral random projections to directly obtain the low-rank component while RNMF decompose a sparse component in the NMF decomposition to speed up the SVD operation.

1.2 Contributions

Traditional clutter removal methods are quite successful for clutter removal tasks. However, running these algorithms requires knowledge of numerous parameters. These parameters vary from one application to another, making them inflexible. Additionally, the traditional methods involve a high number of iterations and computational costs, making them unsuitable for real-world applications.

In this thesis, instead of traditional algorithms, deep learning algorithms are proposed to remove clutter in GPR images. The algorithms we proposed are Learned RPCA (LRPCA), Convolutional Robust Principal Component Analysis (CORONA), and GODEC-Net, respectively. The contributions can be summarized as follows::

- LRPCA [25] extends deep unfolding from finite iterations to infinite iterations via a novel feedforward-recurrent-mixed neural network model. Experimental results show that LRPCA can speed up the run-time in the test phase compared to other traditional methods and it makes hyperparameters are learnable.
- CORONA [26] is an advanced unfolding algorithm that effectively minimizes the number of iterations within the iterative algorithm and exhibits excellent

performance in clutter removal tasks. Each iteration can be replaced by a convolutional layer instead of fully connected layers. Also, convolutional layers decrease the number of learnable parameters therefore algorithm is accelerated.

- Although, CORONA is a fast algorithm, its computational intensity is increased by the use of Singular Value Decomposition (SVD) in every iteration. However, the newly proposed method, GODEC-Net, enhances the speed of the algorithm by employing bilateral random projections (BRP) instead of SVD at each iteration. This leads to an increase in the speed of regular operations for CORONA, as detailed in the publication.
- The proposed methods are evaluated on a newly generated real GPR dataset created under different scenarios.

1.3 Thesis Outline

Chapter 2 provides a comprehensive overview of the working principle of GPR, its applications, and the causes of clutter. Additionally, it discusses traditional methods for clutter removal. Recognizing the computational cost and run-time limitations of these traditional approaches, Chapter 3 introduces three alternative unfolded methods: LRPCA, CORONA, and GODEC-Net. The architectural details of these proposed methods are thoroughly described. In Chapter 4, an experimental study is conducted using a new real GPR dataset, where both the traditional methods and the proposed method are implemented and evaluated. Finally, Chapter 5 discusses the conclusions drawn from the study and proposes directions for future research.

2. CLUTTER REMOVAL METHODS FOR GPR IMAGES

2.1 Ground Penetrating Radar (GPR)

Ground penetrating radar is technique that is used to explore underground objects. In essence, the GPR system can be conceptualized as comprising four main elements: a central unit, a transmitting antenna, a receiving antenna, and a computer. The central unit generates an electromagnetic signal, which is then emitted into the ground through the transmitting antenna. The electromagnetic signal is emitted in all directions, although a significant portion of its energy is focused within a cone-shaped region beneath the antenna, as depicted in Figure 2.1. If the electromagnetic waves encounter any buried disruption such as an underground object or the boundary between two geological layers, a cavity, an area with varying moisture levels, etc., they will scatter in various directions in a specific pattern, which is determined by the particular underground conditions. Then, all signals reflected from the target are received by the receiving antenna.

It is considered to be transmitter and receiver antennas are in same unique box and move together. The collected signal from buried objects is displayed simultaneously on the screen. A GPR system typically includes cables that connect the central unit, antennas, and computer, as well as a field energy source such as rechargeable batteries. The central unit converts the electrical energy from the batteries into a microwave signal. GPR signals are expressed in three different ways. The trace means that when GPR data is collected at a specific location, it's called an A-scan or a GPR trace shown in Figure 2.2. On the other hand, when all the GPR traces collected along a line are put together, it's called a B-scan and shown in Figure 2.3. C-scan is created by putting together multiple B-scans. In other words, a C-scan is a compilation of B-scans. The A-scan result is a signal that is taken at any time. B-scans are generated by systematically moving the GPR across a surface in a specific direction while collecting

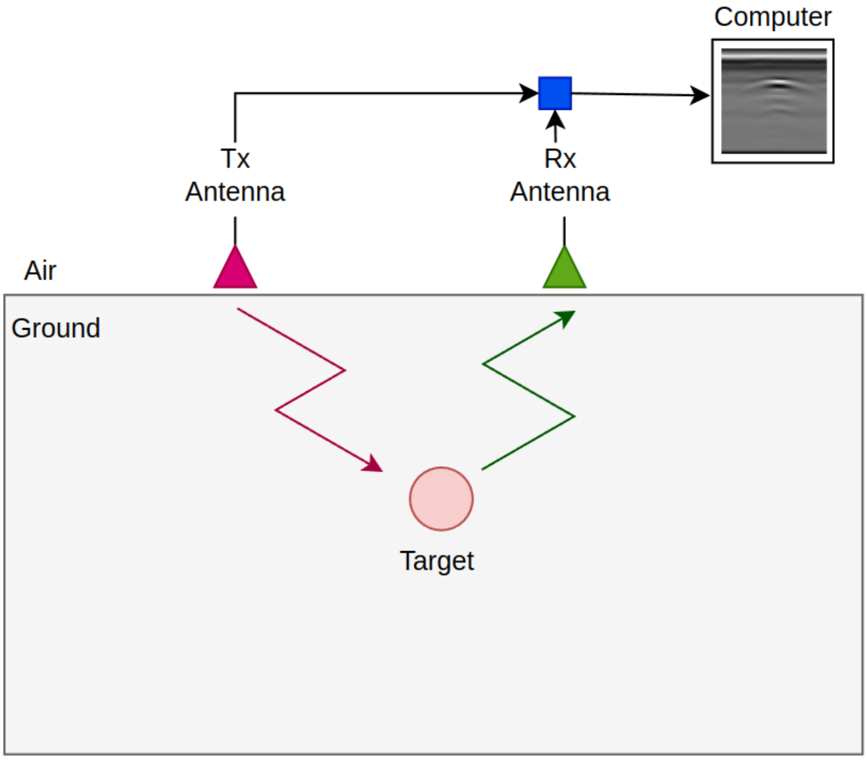

Figure 2.1 : Architecture of GPR.

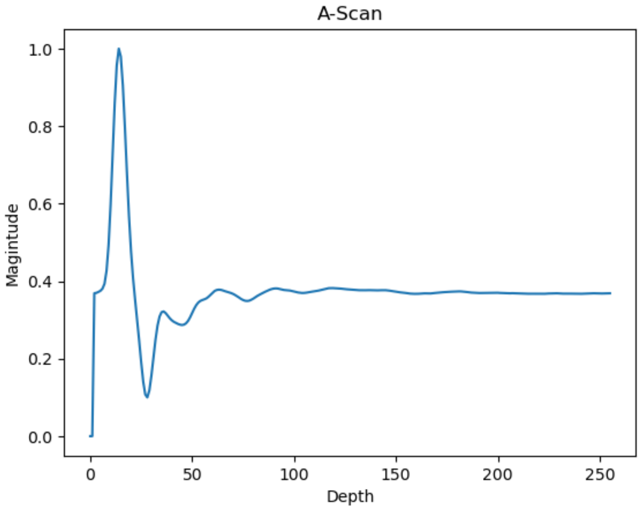

Figure 2.2 : A-Scan GPR.

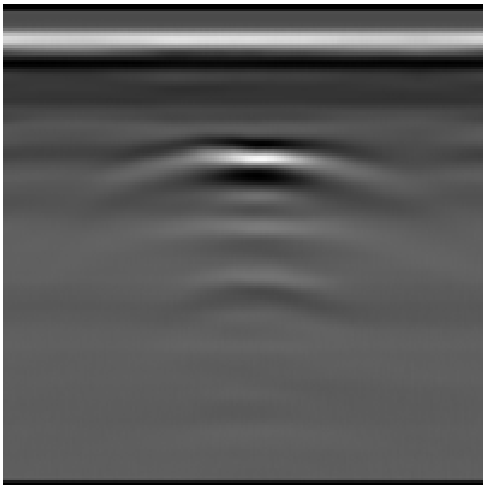

Figure 2.3 : B-Scan GPR Image.

A-scans at pre-defined spatial intervals. This process generates data represented as two-dimensional views or images. When data is collected over a surface, it is referred to as a C-scan and illustrated in Figure 2.4. This data is typically presented and analyzed as slices of B-scans. It is crucial to highlight that information can be acquired at different elevations above the ground.

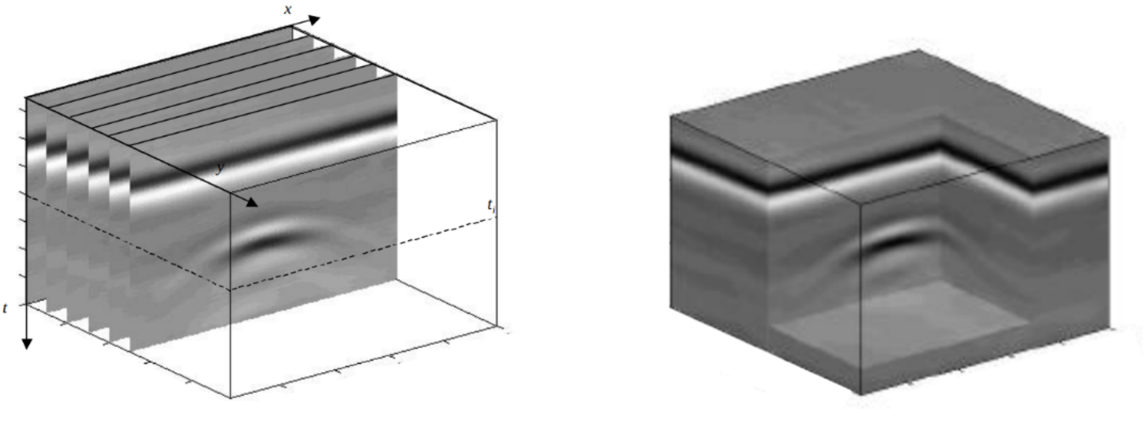

Figure 2.4 : C-Scan GPR Image.

2.1.1 GPR applications

The GPR can be used many research areas such as, mineral exploration [1], mining [27], environmental management [28], archaeological survey [29], landmine detection and grave location [30].

Mineral exploration is essential for the identification and extraction of valuable resources from beneath the Earth's surface. GPR has become a potent geophysical instrument in this field, owing to its capability to detect and analyze subsurface geological structures and mineral deposits. The Figure 2.5 demonstrates a typical mineral exploration application with GPR.

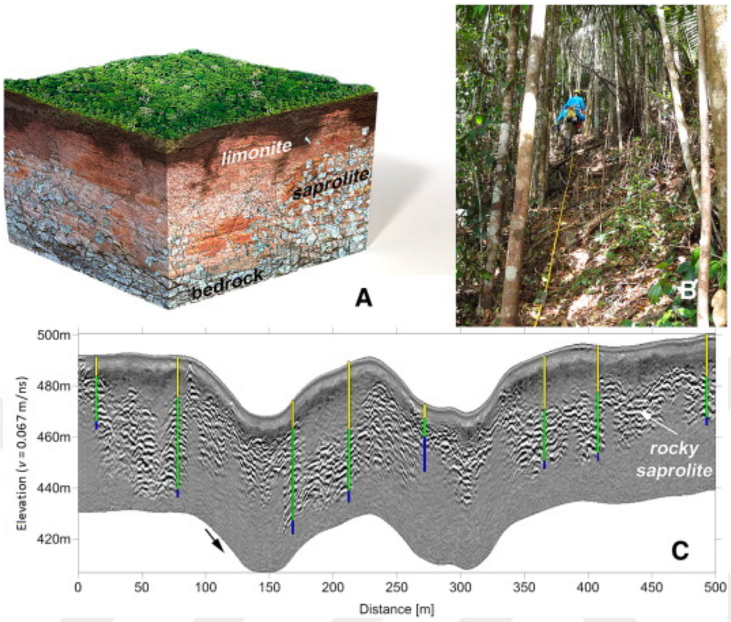

Figure 2.5 : Illustration of mineral exploration application with GPR [1], (a) representation of a nickel laterite profile, (b) surveying area, (c) A radar profile at 30 MHz depicting the presence of rocky saprolite within the profile.

Figure 2.5 (a) illustrates the characteristic zone, displaying the close proximity of the limonite plate to the Earth's surface, followed by the presence of the saprolite and bedrock plates. In Figure 2.5 (c), the limonite zone is represented by the yellow line, the saprolite zone by the green line, and the bedrock zone by the blue line.

Currently, GPR is used to generate high-resolution images of mining activities. To effectively prevent structural damage in mining operations, mining engineers require comprehensive knowledge regarding the bulk properties of the surrounding rock mass. [31]. GPR can offer valuable insights into the distribution, shape, size, aperture, and orientation of fracture discontinuities. This knowledge is essential for the development of effective remediation strategies.

Ground-penetrating radar surveys enable extensive coverage of large areas within a short time-frame while providing exceptional spatial resolution for detecting buried archaeological features and their associated stratigraphy. Figure 2.6 illustrates an archaeological survey conducted in Ashkelon, Israel.

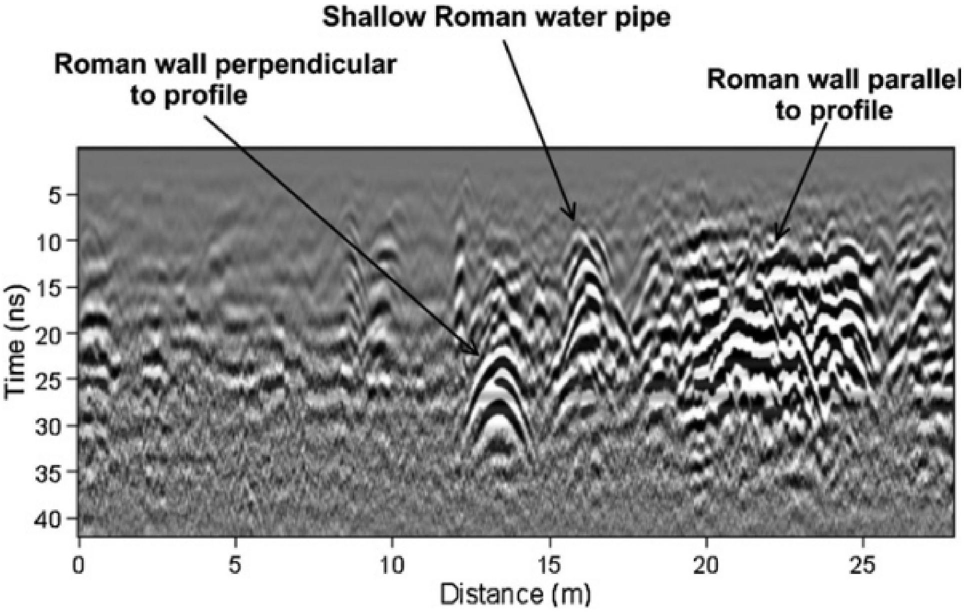

Figure 2.6 : The GPR reflection profile illustrates the Roman remains discovered in Ashkelon, Israel [2].

Landmines pose a humanitarian challenge as they cause indiscriminate casualties and injuries among civilians. These weapons lack the ability to differentiate between military personnel and innocent civilians, and their destructive potential persists for many years [32].

2.2 Clutter in GPR Systems

Ground Penetrating Radar (GPR) finds extensive application in the detection of subsurface objects, including landmines, minerals, and cables. To investigate the subsurface, GPR antennas transmit electromagnetic signals to the ground and the antennas receive signals reflected from different underground objects. The signals that bounce back are influenced by numerous factors like soil composition, moisture levels, presence of gravel, and other unfamiliar objects. Additionally, direct interaction between the transmitting and receiving antennas in ground-penetrating radar (GPR) can lead to unwanted interference, resulting in cluttered scans. The clutter is preventing to detect targets and decreases the performance of detection algorithms since it is

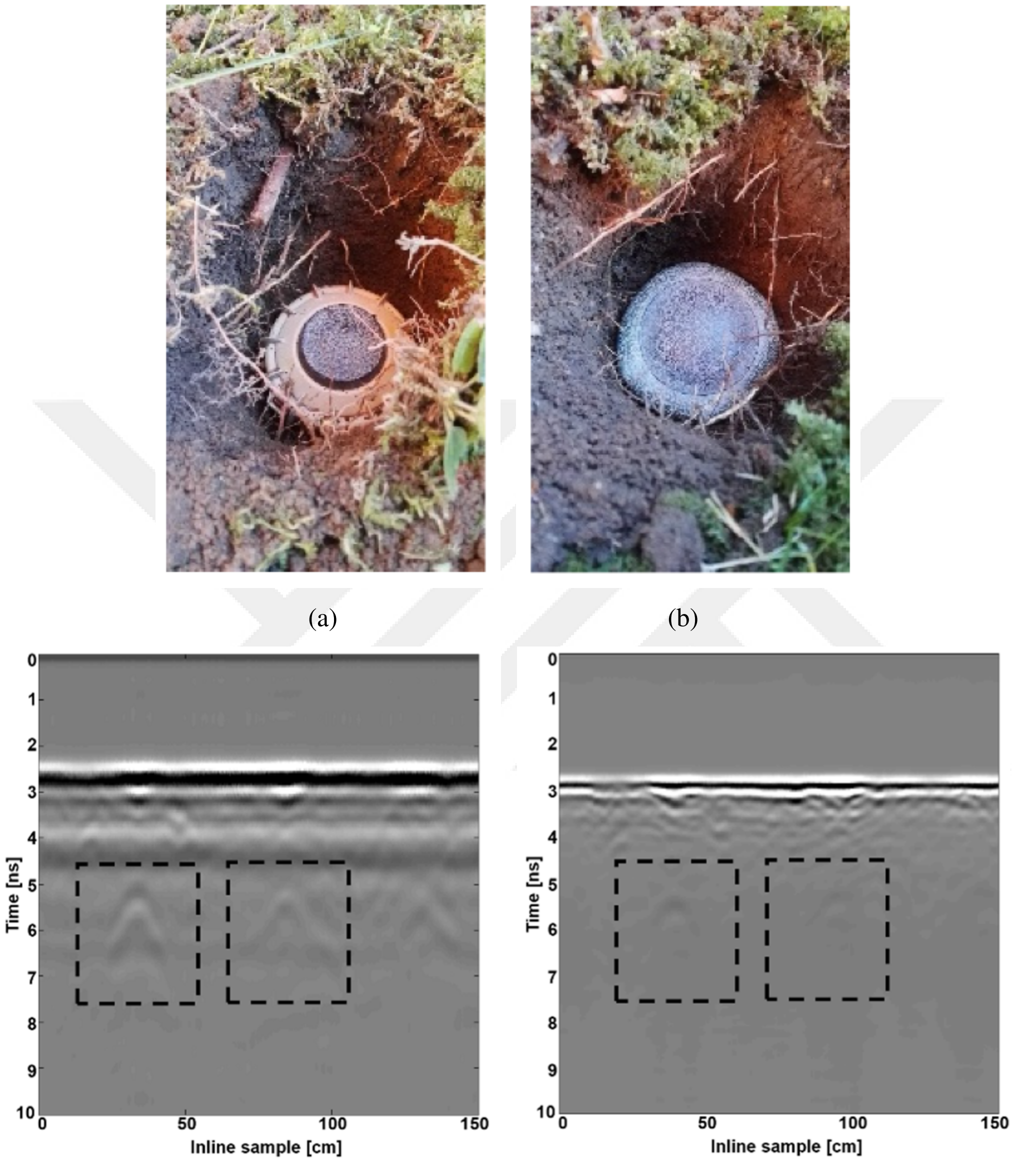
(a) (b)

(c) (d)

Figure 2.7 : Illustration of experimental landmine detection, (a) represents VS-50 landmine, (b) shows SB-33 landmine, The B-Scan images of landmines is depicted in (c) and (d), respectively [3].

dominating targets' reflections. Therefore, clutter removal of GPR images is crucially important for detecting underground objects.

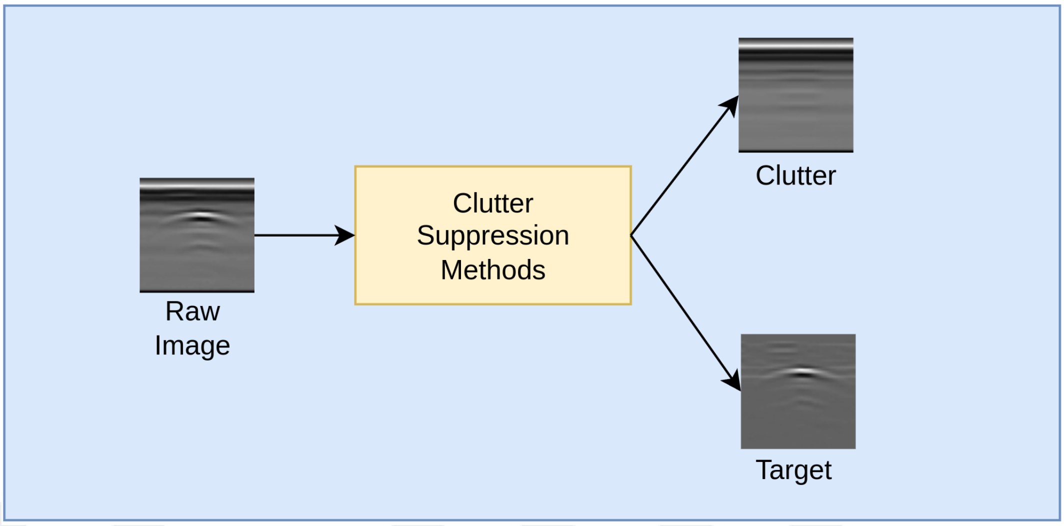

Figure 2.8 : Clutter removal methods basic diagram.

Figure 2.8 illustrates the fundamental diagram of clutter removal methods. These methods are employed to remove clutter from raw GPR images. Through a series of mathematical operations, the raw image is decomposed into clutter and target components. Figure 2.8 visually demonstrates how clutter removal methods effectively eliminate clutter, allowing the target to be clearly detected.

2.3 SVD

SVD is used many application such as, image processing [33], noise reduction [34] and clutter removal [35]. The SVD factorizes a matrix into three separate matrices, resulting in a diagonal matrix of singular values. Let's define the GPR image as $X_{i,j} \in R^{M\times N}$, where M refers number of data point in each A-scan trace, and N denotes number of traces, when using SVD for the purpose of removal clutter in GPR images. In this context, the index i refers to the depth, while the index j refers to the position of the antenna or the down-track. The SVD decomposition of the data matrix X can be expressed as follows,

$$X = USV^{\top} \tag{2.1}$$

In equation (2.1), U and V represent orthogonal matrices that correspond to the left and right singular vectors, respectively. In other words, U and V are the eigenvectors of

$XX^\top$ and $X^\top X$, while S is diagonal matrix and represented as $S = diag(\sigma_1, \sigma_2, ..., \sigma_r)$. The SVD decomposition is,

$$X = \sum_{i=1}^{N} = \sigma_i u_i v_i^\top \tag{2.2}$$

$$X = M_1 + M_2 + ... + M_N \tag{2.3}$$

M_i represents matrices that have the same dimensions as X and are referred to as the eigenimages corresponding to the ith component of X. The data matrix X consists of a combination of clutter and target matrices. Hence, it can be divided into two distinct subspaces, target and clutter such as,

$$X = X_C + X_T = \sigma_1 u_1 v_1 + \sum_{i=2}^{N} = \sigma_i u_i v_i^\top \tag{2.4}$$

where, X_C represents clutter, while X_T depicts target matrix of GPR image.

2.4 RPCA

Principal Component Analysis (PCA) is used in different applications such as, image processing, dimensionality reduction and facial recognition. The PCA method separates the data into uncorrelated components, and it is one of the methods used to separate clutter, target, and noise in GPR images, which are noise reduction techniques. Nevertheless, in order to achieve optimal results, the subspace techniques necessitate accurate determination of the clutter subspace. In most cases, clutter is seen as the primary element in GPR images because it tends to have a stronger presence compared to the signal reflected by the target. Consequently, the target is regarded as the secondary element in these images. In situations where there are multiple targets, it may be possible to extract information about the targets from several components, rather than just one, or the components may not be sorted in descending order. Over the course of many years, numerous natural methods for enhancing the robustness of PCA have been investigated and suggested in academic literature such as influence function techniques [36] and alternating minimization [37]. An idealized version of Robust PCA is a decomposes corrupted matrix as low-rank and sparse components. Let define GPR matrix X as,

$$X = L + S + N \tag{2.5}$$

where L is low-rank matrix, S is a sparse matrix and N is a random noise matrix. RPCA decomposes GPR images as low-rank and sparse component minimizing the following equation,

$$\underset{L,S}{min}||L||_* + \lambda||S||_1 \quad \text{s.t} \quad ||X-L-S||_F \leq \delta \tag{2.6}$$

In equation (2.6), the notation $||.||_*$ corresponds to the nuclear norm, which involves adding up the singular values of L, $||.||_1$ denotes the L_1-norm, which is sum of the absolute value of non-zero elements, λ is the regularization parameter. The S component is obtained through soft thresholding, then the X component is obtained through singular value thresholding.

2.5 RNMF

Robust NMF (RNMF) [38] is a technique that divides the corrupted data matrix, represented as X, into two parts: a sparse matrix and the outcome of multiplying two non-negative matrices, W and H,

$$X \approx WH + S \tag{2.7}$$

where $X \in R^{M\times N}$, $W \in R^{M\times k}$, $H \in R^{k\times N}$, and $S \in R^{M\times N}$, k is similar the rank of factorization in NMF. The minimization problem of RNMF can be written as,

$$\underset{W,H,S}{min}||X-WH-S||_F^2 + \lambda||S||_1 \quad \text{s.t} \quad W \geq 0 \tag{2.8}$$

Here $||.||_F$ stands for the Frobenious, and $||.||_*$ is the nuclear norm and λ is hyperparameter.

RNMF obtains W and H through iterative updates as,

$$W_{i,j} \leftarrow \Big[\frac{|((S-X)H_T)_{i,j}| - ((S-X)H_T)_{i,j}}{2(W^TWH^T)_{i,j}}\Big]W_{i,j} \tag{2.9}$$

$$H_{i,j} \leftarrow \Big[\frac{|(W^T(S-X))_{i,j} - (W^T(S-X))_{i,j}}{2(W^TWH)_{i,j}}\Big]H_{i,j} \tag{2.10}$$

where W and H can be normalized as,

$$W_{i,j} \leftarrow \frac{W_{i,j}}{\sqrt{\sum_{r=1}^{n} W_{k,j}^{2}}} \tag{2.11}$$

$$H_{i,j} \leftarrow H_{i,j}\sqrt{\sum_{r=1}^{n} W_{k,j}^{2}} \tag{2.12}$$

To achieve the optimal sparsity parameter, S, it is necessary to maintain a constant state for both W and H. S can be updated as following equation,

$$s \leftarrow T_{\frac{\lambda}{2}}(X - WH) \tag{2.13}$$

The sparse component of the GPR image is represented as $X_{clutter} = S$, while the low-rank component is represented as $X_{target} = WH$. During each iteration, updates are performed on W, H, and S based on equations (2.12) and (2.13). The process continues until a stopping criterion is met, which can be either reaching the maximum iteration number or a selected threshold or. The resulting S matrix represents the target region of the GPR image.

2.6 RAE

In this section, we will discuss an unsupervised-based method called Robust AutoEncoders (RAE) that differs from traditional clutter removal methods. RAE utilizes autoencoders, which are commonly employed for tasks such as anomaly detection, image compressing, recommendation systems and clutter removal in GPR images. The architecture of the autoencoder (AE) is depicted in Figure 2.2, illustrating its three layers. The encoder's primary function is to significantly decrease the dimensionality of the input data, denoted as X, and produce a condensed representation called H within a lower-dimensional latent space. This compressed representation is essential for efficient data processing and storage. Conversely, the decoder takes the compressed representation H and performs an inverse mapping to reconstruct the original input. Robust AE decomposes a sparse matrix using the l_1-norm, similar to RPCA, but it also utilizes the non-linear representation capability of an autoencoder to capture the low-rank component. This makes RAE more efficient than RPCA in

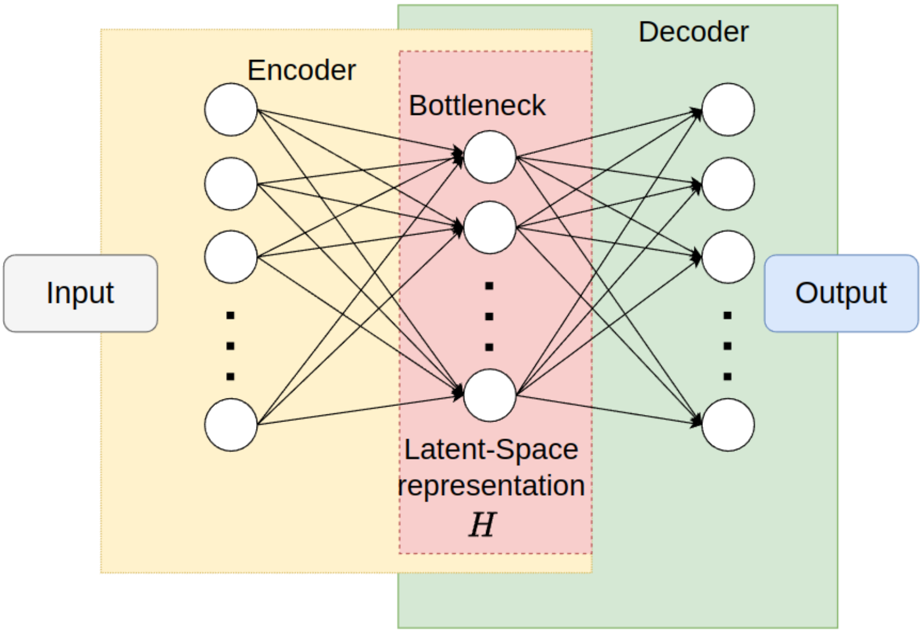

Figure 2.9 : Typical Autoencoder scheme.

handling irregular clutter situations. The RAE equation (2.6) is solved as follows,

$$\underset{L,S}{min}||L-D(E(L))||_1+\lambda||S||_1 \quad \text{s.t} \quad ||X-L-S||_F \leq \varepsilon \tag{2.14}$$

RAE uses alternating directions method (ADM) to solve equation (2.14),

$$\begin{aligned}\mathscr{L}(L,S,Y) = ||L-D(E(L))||_2+\lambda||S||_1+\langle Y, X-L-S\rangle \\ +\frac{\beta}{2}||X-L-S||_F\end{aligned} \tag{2.15}$$

In this context, the terms Y and β represent the Lagrange multiplier and the over-regularization parameter, respectively. Additionally, $\langle . \rangle$ denotes the inner product operation. The equation (2.15) can be solved in three steps. First, $min_L \mathscr{L}(L,S,Y)$ is solved using autoencoder which is trained by the back-propagation method. Second, to solve $min_S \mathscr{L}(L,S,Y)$ is used proximal method. The third step involves updating the Lagrange multiplier Y using the residual between X, L, and S.

2.7 GoDec

RPCA is commonly used to separate the low-rank and sparse components of GPR images. However, since RPCA requires a high computational cost due to the singular value decomposition (SVD) operation in each iteration to solve non-convex minimizing operations, this increases the runtime. In 2011, researchers proposed a rapid solution to Equation (2.6) called Go Decomposition (GoDec) [18], which employs bilateral random projection (BRP) as described in their paper. This method enables the decomposition of X into low-rank and sparse components through minimization,

$$\overset{min}{_{L,S}}||X-L-S||_F^2 \quad s.t \quad rank(L) \leq r, card(S) \leq k \tag{2.16}$$

In this context, the term rank(L) refers to the number of linearly independent rows or columns in the matrix L, while card(S) represents the count of non-zero elements in S. The equation (2.16) can be solved iteratively by optimizing two sub-problems, as presented

$$\begin{aligned} L_t &= \overset{argmin}{_{rank(L)\leq r}}||X-L-S_{t-1}||_F^2 \quad and \\ S_t &= \overset{argmin}{_{card(S)\leq k}}||X-L_t-S||_F^2 \end{aligned} \tag{2.17}$$

until convergence is achieved. During each iteration, the L_t component is updated through singular value hard thresholding of $X-S_t$, while the S component is updated by employing entry-wise hard thresholding of $X-L_t$. GoDec uses an alternating approach to assign the r-rank approximation of X to S, and the sparse approximation of X with cardinality k to L.

The procedure presented in equation (2.6) can be expedited by substituting the computationally expensive SVD operation with BRPs (Bilateral Random Projections) [10]. To perform r BRPs on a dense matrix X with dimensions M x N , two sets of random vectors are created, A_1 and A_2, and use them to generate left and right random projections, Y_1 and Y_2, respectively. To improve the left and right projection matrices, the right random projection Y_1 is employed to construct a more refined A_2, while Y_2 is used to construct a better A_1. Specifically, after obtaining Y_1 through $Y_1 = XA_1$, A_2 is updated as $A_2 = Y_1$. Similarly, to compute the left random projection Y_2, we set $Y_2 = X^TA_2$ and update A_1 as $A_1 = Y_2$. By utilizing the updated Y_1 and Y_2, a more accurate low-rank approximation L can be obtained. By using these updated projections, we can obtain a better low-rank approximation L of the original matrix X.

$$L = Y_1(A_2^T Y_1)^{-1} Y_2^T \tag{2.18}$$

As a result, calculation of L with Equation (2.18) reduces computational cost. Under certain favorable conditions, the error of approximation using BRP approaches can be comparable to the error of approximation using SVD.

3. PROPOSED METHODS

3.1 Background on Unfolding

The technique of unrolling an algorithm was initially proposed by Gregor et al. [39] with the goal of reducing the computational expenses of sparse coding. Unrolling methods can be universally employed with iterative algorithms. This technique converts an iterative algorithm into a deep neural network by representing each iteration as a singular network layer and subsequently combining these layers in a finite sequence. Furthermore, this process enables the parameters of the original iterative algorithm to be learned through the unfolding algorithm.

The unfolded algorithms are used fewer hyperparameters when it compared with other neural networks. This reduction is achieved by incorporating domain knowledge through the unrolling process. Furthermore, the structures of unrolled networks are specifically designed to suit target applications. This approach not only enhances efficiency but also improves flexibility, particularly in scenarios where training data is limited.

Figure 3.1 depicts the top-level representation of an unrolled network. The left side of the figure illustrates the iterative algorithm, while the right side demonstrates the unrolling algorithm. In the iterative algorithm, the symbol h represents iterations, and θ represents the parameter of h. In the unrolled network, each iteration h can be considered as a layer. Unlike the iterative algorithm where θ needs to be known beforehand for optimal performance, the unrolling algorithm allows θ to be learned within each layer. The learnable parameters in Figure 3.1 are highlighted in blue color.

Iterative algorithms are not suitable for real-world applications due to their high number of iterations and slow execution. By converting iterative algorithms into unrolled networks and training them on datasets, they can be utilized for real-world applications. In this study, three different unfolded algorithms were proposed.

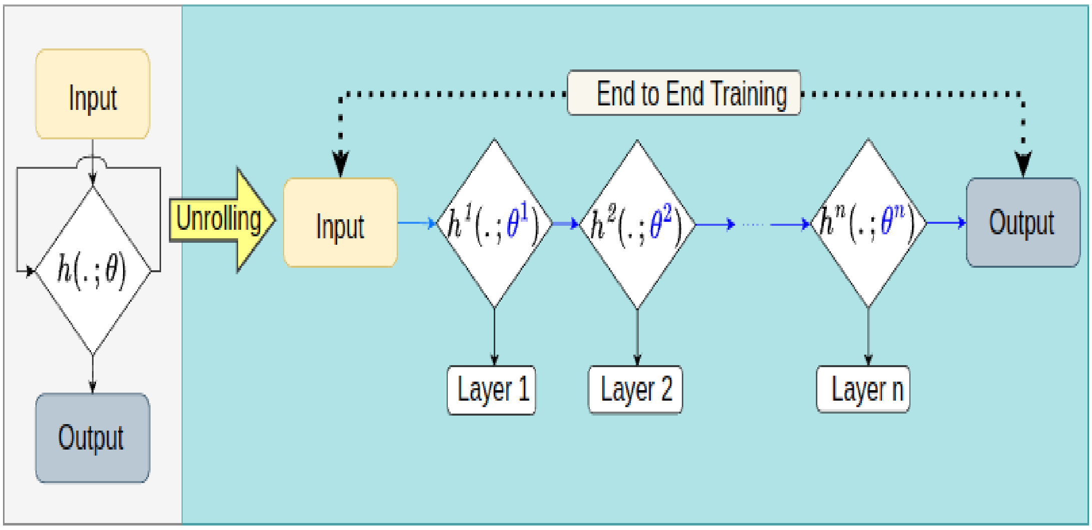

Figure 3.1 : Illustration of top level unfolded network.

3.2 LRPCA

Let the B-scan images of Ground Penetrating Radar (GPR) be represented by $Y \in R^{M \times N}$, where M and N denote the sample numbers for space and time, respectively. The B-scan GPR data Y consists of clutter and target components. In GPR imaging, the echoes that bounce back from things other than the intended target, such as rocks, roots, or other small changes in the ground, are considered as background noise. The actual target being searched for, on the other hand, can be considered as the sparse component. Thus, GPR matrix Y is formulated as,

$$Y = X + S + N \tag{3.1}$$

where X is low-rank matrix, S is a sparse matrix and N is a random noise matrix. In earlier works, the minimization problem can be described as

$$\underset{X,S}{min} ||X||_* + \lambda ||S||_1 \tag{3.2}$$

where $||.||_*$ stands for the nuclear norm, which sums the singular values of X, $||.||_1$ is the l_1-norm, ie. sum of the absolute value of non-zero elements, the parameter λ serves as the regularization parameter. The S component is obtained through soft thresholding, and the X component is obtained through singular value thresholding. Existing convex approaches for RPCA can decompose the low-rank and sparse components exactly. However, the computational cost of such algorithms is still high per iteration.

One way to approach the problem is by using the Alternating Projections (AltProj) method. To achieve this, the process alternates between projecting the matrix difference $Y - S$ onto the set of low-rank matrices, and projecting the matrix difference $Y - X$ onto the set of sparse matrices. A more efficient approach called AccAltProj has been suggested for RPCA, which accelerates the current alternating projections method and greatly improves its computational efficiency.

The reformulation of X as $X = LR^\top$ significantly improves computational efficiency, as it allows for the use of SVD just in the initialization step. The gradient descent (GD) is then applied to L and S to update them at each iteration. However, the convergence rate of GD is dependent on κ. To overcome this dependency, ScaledGD [40] was introduced. LRPCA solves the minimization problem similarly to ScaledGD but with different sparsity constraints. It can be formulated as follows,

$$\underset{L,R,S}{min} \frac{1}{2}||LR^\top + S - Y||_F^2, \quad \text{subject to supp}(S) \subseteq \text{ supp}(S_*) \tag{3.3}$$

where $||.||_F$ stands for the fabinous norm. The LRPCA algorithm does not require an exact estimate of α, as in ScaledGD. Moreover, it can effectively remove incorrect outlier detections during each step of the detection process.

Algorithm 1 GPR image separation by LRPCA

```
$Input$ : $Y$ : raw GPR image, $r$: the rank the low-rank matrix, $\zeta_k$ : learned thresholding values, $\eta_k$ :learned step sizes
$Initalize$
$S_0 = \mathscr{S}_{\zeta_0}(Y)$
$[U_0, \Sigma_0, V_0] = SVD_r(Y - S_0)$
$L_0 = U_0 \Sigma_0^{1/2} \quad R_0 = V_0 \Sigma_0^{1/2}$
$Updates$
while Not do
    $S_{k+1} = \mathscr{S}_{\zeta_{k+1}}(Y - L_k R_K^\top)$
    $L_{k+1} = L_k - \eta_{k+1}(L_k R_K^\top + S_{k+1} - Y) R_k (R_k^\top R_k)^{-1}$
    $R_{k+1} = R_k - \eta_{k+1}(L_k R_K^\top + S_{k+1} - Y)^\top L_k (L_k^\top L_k)^{-1}$
end while
$Output : X_K = L_K R_K^\top$ : the low-rank matrix, $S_K$ : the recovered sparse matrix
```

Algorithm (1) outlines the architecture of the LRPCA algorithm, which can be divided into two main parts: initialization and iterative updates. During initialization, a

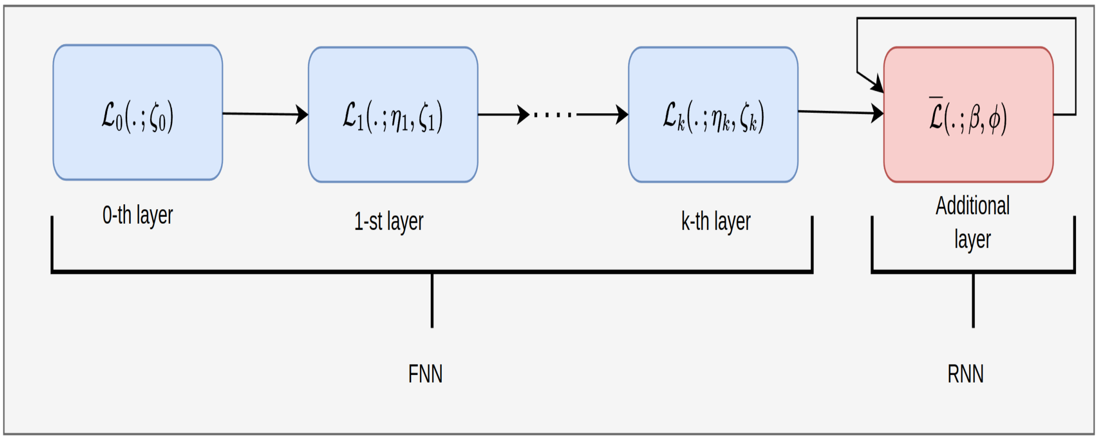

Figure 3.2 : Illustration of LRPCA network.

modified spectral method is used to obtain the sparse matrix $S_0 = \mathscr{S}_{\zeta_0}(Y)$, which removes obvious outliers via soft thresholding. The low-rank component is then acquired using SVD, resulting in $L_0 = U_0\Sigma_0^{1/2}$ and $R_0 = V_0\Sigma_0^{1/2}$. In the iterative updates phase, the sparse component is updated using simple soft thresholding, with $S_{k+1} = \mathscr{S}_{\zeta_{k+1}}(Y - L_k R_K^\top)$.

With appropriate threshold values, this method can guarantee linear convergence and can even converge faster than ScaledGD while still satisfying the same assumptions. To update the low-rank component, gradient descent is applied to L and R at each iteration.

Figure 3.2 shows the LRPCA architecture. In this architecture, $\mathscr{L}_k$ represents each feed-forward neural network layer, and $\overline{\mathscr{L}}$ represents the recurrent neural network layer. Deep unfolding algorithms often unfold iterative algorithms into a fixed number of layers, which can limit the model's flexibility and accuracy. To address this issue, LRPCA incorporates an Recurrent Neural Network (RNN) layer into the fixed-layer Fedforward Neural Network (FNN) model, resulting in an infinite-layer model known as the feedforward-recurrent-mixed neural network (FRMNN). Training the FRMNN involves two stages. First, the K-layer FNN is trained with layer-wise training, and the parameters $\{\zeta_k\}$ and $\{\eta_k\}$ are learned. Afterwards, the objective is to find the optimal values of β and ϕ that minimize the convergence matrix in the RNN. As a result, FRMNN is capable of efficiently learning the parameters for infinite iterations of

LRPCA without experiencing the usual decrease in performance that is often observed in traditional deep unfolding methods.

3.3 CORONA

In this section, the minimization problem is formulated as,

$$\underset{L,S}{min}\frac{1}{2}||X-(L+S)||_F^2+\lambda_1||L||_*+\lambda_2||S||_{1,2} \tag{3.4}$$

where $||.||_F$ denotes the Frobenious norm,$||.||_*$ stands for the nuclear norm, which sums the singular values of L, $||.||_{1,2}$ norm, which sums the $l_{1,2}$ norms of each row of S, and λ_1 and λ_2 are hyperparameters. A generalized form of the Iterative Shrinkage-Thresholding Algorithm (ISTA) can be employed to resolve the optimization problem defined in equation (3.4) and the iterative algorithm updates at iteration $k+1$ for L^{k+1} and S^{k+1} using the alternating proximal gradient method. It can be updated following equation,

$$\begin{aligned} L^{k+1} &= SVT_{\lambda_{1/2}}\Big(\frac{1}{2}L^k-S^k+X\Big) \\ S^{k+1} &= \mathscr{T}_{\lambda_{1/2}}\Big(\frac{1}{2}S^k-L^k+X\Big) \end{aligned} \tag{3.5}$$

In each iteration, L^{k+1} is updated via singular value thresholding (SVT) algorithm, and soft thresholding has been applied to update S^{k+1}.

The iterative algorithm performs well in clutter removal applications. However, proper selection of λ_1 and λ_2 parameters is required, and this may vary from one application to another. Additionally, the iterative algorithm is not suitable for real-world applications because it requires a large number of iterations to solve the problem. These constraints have led to the proposal of solutions where the hyperparameters are automatically learned, resulting in solutions that require less computational cost.

The unfolding neural networks unroll each iteration in an iterative algorithm as layers in a deep neural network. Firstly, the iterative algorithm in equation (3.5) can be rewritten as,

$$\begin{aligned} L^{k+1} &= SVT_{\lambda_{1/2}}\Big(W_1X+W_3S^k+W_5L^k\Big) \\ S^{k+1} &= \mathscr{T}_{\lambda_{1/2}}\Big(W_2X+W_4S^k+W_6L^k\Big) \end{aligned} \tag{3.6}$$

where $W_1 = W_2 = I, W_3 = W_6 = -I$, and $W_4 = W_5 = \frac{1}{2}I$. CORONA uses convolutional kernels instead of matrix multiplication, thus the number of learnable hyperparameters is reduced. The process of matrix multiplications is substituted with 2D convolution kernels $W_1^k, ..., W_6^k$ that are learned during the training of the entire network. Finally, the deep network can be written as,

$$\begin{aligned} L^{k+1} &= SVT_{\lambda_1^k}\left(W_1^k * X + W_3^k * S^k + W_5^k * L^k\right) \\ S^{k+1} &= \mathscr{T}_{\lambda_2^k}\left(W_2^k * X + W_4^k * S^k + W_6^k * L^k\right) \end{aligned} \tag{3.7}$$

where * operator represents convolution operators. In the training phase, hyperparameters λ_1^k and λ_2^k are learned for each layer.

Figure 3.3 shows a visual representation of unfolded deep network architecture. The iterative algorithm is converted to a deep network layer, and blue boxes (λ_1, λ_2) are learned in the training phase.

CORONA aims to recover both L and S using back-propagation as other supervised deep networks. To train the model, we used a real GPR image dataset which includes raw images as X, low-rank component L, and sparse component S both are generated from traditional RPCA. The loss function in the training phase is the mean squared error that measures mean differences between predicted S and L values of the network and $\hat{S}$, $\hat{L}$, respectively.

$$\begin{aligned} \mathscr{L}(\theta) = &\frac{1}{2N}\sum_{i=1}^{N} ||f_S(X_i, \theta) - \hat{S}_i||_F^2 \\ &-\frac{1}{2N}\sum_{i=1}^{N} ||f_L(X_i, \theta) - \hat{L}_i||_F^2 \end{aligned} \tag{3.8}$$

The loss function can be described as f_S/f_L is sparse/low-rank prediction of CORONA with learnable parameters $\theta = W_1^k, ..., W_6^k, \lambda_1^k, \lambda_2^k, k = 1, ..., K$, where K is the number of chosen layers.

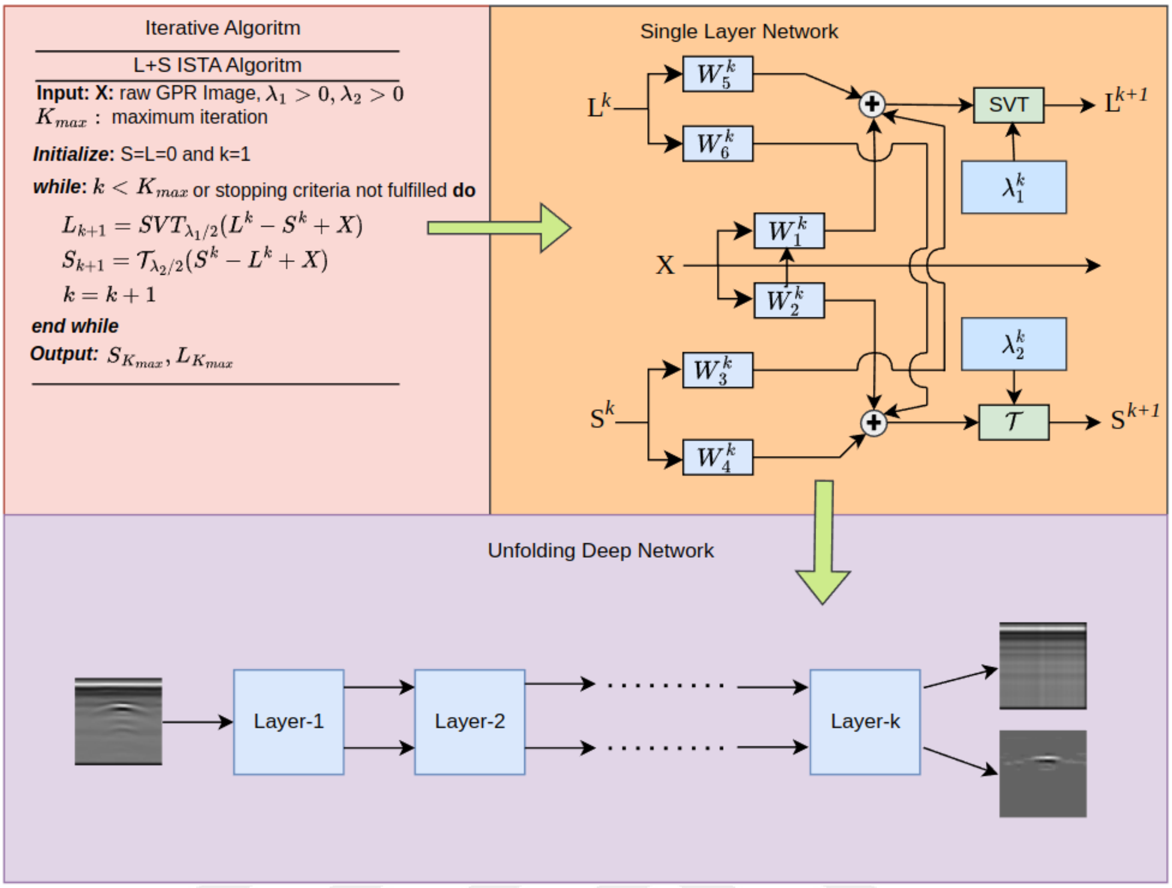

Figure 3.3 : Proposed algorithm architecture.

3.4 GODEC-Net

SVT is a common method used in solving low-rank matrix recovery problems. It's often used in numerical schemes for nuclear norm minimization. The traditional way of performing SVT involves finding SVD and then shrinking the singular values. However, this approach can be slow, particularly if the rank of the matrix is not significantly lower than its dimension. CORONA uses SVT to update L^{k+1} in each iteration. Thus, we propose a new method that can speed up the training time of CORONA by replacing SVT in each batch with BRP. The proposed algorithm's architecture is presented in Figure 3.4. In this diagram we calculate BRP instead of SVT to update L^{k+1}. Thus, Bilateral random projections (BRP) can greatly speed up the algorithm.

$$\begin{aligned} L^{k+1} &= BRP_{\lambda_1^k}\{W_5^k * L^k + W_3^k * S^k + W_1^k * X\} \\ S^{k+1} &= \mathcal{T}_{\lambda_2^k}\{W_6^k * L^k + W_4^k * S^k + W_2^k * X\} \end{aligned} \tag{3.9}$$

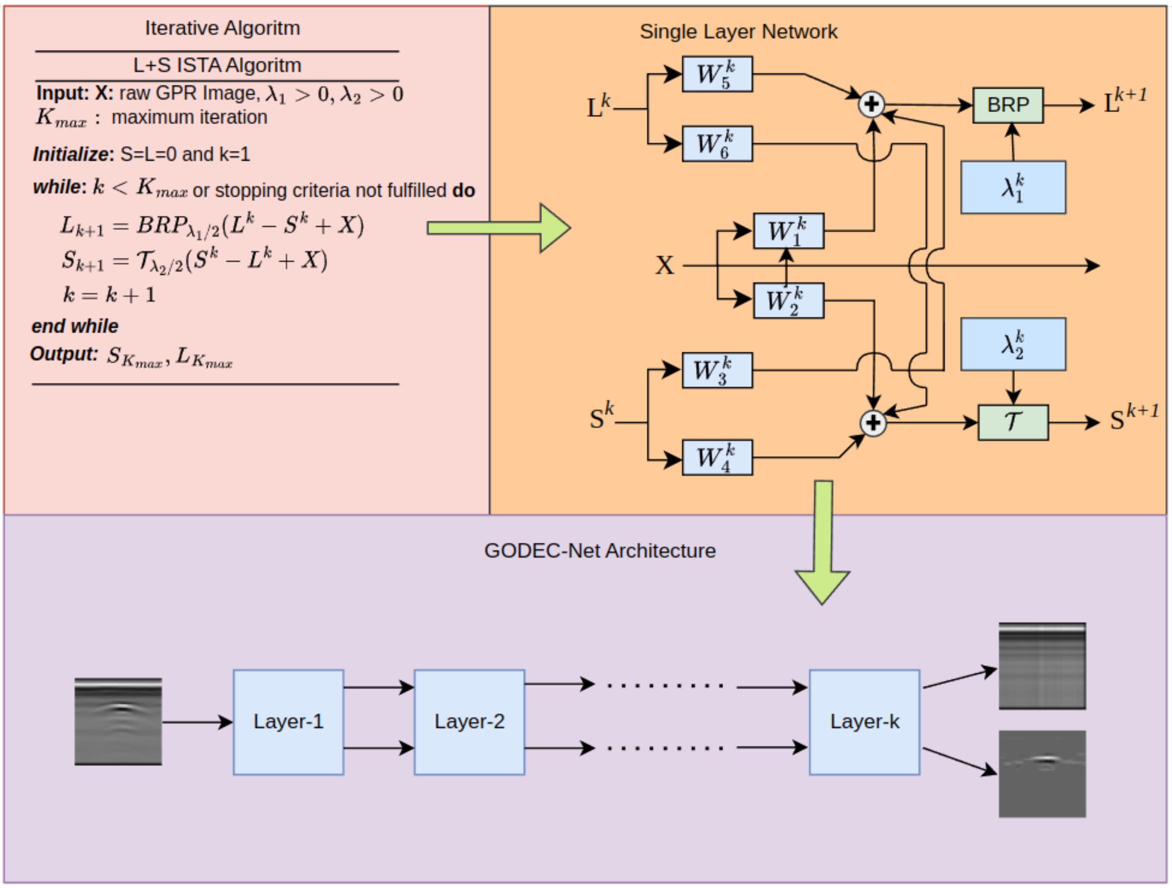

```
Input: X: raw GPR Image, $\lambda_1 > 0, \lambda_2 > 0$
$K_{max}$ : maximum iteration
Initialize: S=L=0 and k=1
while: $k < K_{max}$ or stopping criteria not fulfilled do
    $L_{k+1} = BRP_{\lambda_1/2}(L^k - S^k + X)$
    $S_{k+1} = \mathcal{T}_{\lambda_2/2}(S^k - L^k + X)$
    $k = k + 1$
end while
Output: $S_{K_{max}}, L_{K_{max}}$
```

Figure 3.4 : GODEC-Net architecture.

4. EXPERIMENTAL RESULTS

In this section, the comparison of the three proposed methods with various conventional clutter removal techniques is demonstrated. Two different datasets are used for evaluating the methods. One of them is the hybrid dataset (CLT-GPR), obtained by combining real and simulated datasets. The other dataset is the Real-GPR dataset, created using different scenarios in a real environment and under varying conditions.

The performance of the proposed methods is evaluated visually and through metric calculations, comparing them with traditional methods and the unsupervised learning method, Robust AutoEncoder (RAE). Furthermore, a comparison is made between the proposed unfolded deep network methods. Additionally, a speed comparison between the traditional methods and the proposed methods is conducted using the test data.

CORONA and GODEC-Net methods are tested on both the hybrid dataset and the Real-GPR dataset we created. CORONA was originally proposed for ultrasound images, but we use this method to remove clutter in GPR images. Later, we accelerate CORONA by replacing the computationally expensive SVD operation with the BRP operation. We compare the speed of the two methods against each other and also provide visual comparisons with conventional methods.

We will evaluate the experimental results separately on two datasets. Specifically, the evaluation will be performed under two main headings: CLT-GPR and Real-GPR. Under these headings, the methods we used will be evaluated separately.

4.1 CLT-GPR Dataset Results

CLT-GPR Dataset [41] that includes concrete subdataset, synthetic subdataset and sand subdataset. A synthetic dataset is generated using the open-source software gprMax [42] [43], encompassing a wide range of scenarios beneath the surface. The simulation incorporates six soil types, four different types of surface, two object types, and three different configurations of subsurface objects, varying in depth and radius. The surface types include rough, grassy, flat and rough surfaces with water. The soil types within the dataset consist of dry sand, damp sand, dry clay soil, wet clay soil, dry loam soil, and heterogeneous soil. The objects embedded in the soil are cylindrical in shape and made of either perfect electric conductor (PEC) or polyvinyl chloride (PVC). Additionally, an experimental dataset was created by collecting clutter-only radargrams in a controlled environment specifically for the sand dataset. These radargrams were then combined with simulated clutter-free images, resulting in hybrid raw GPR images. The hybrid raw images, along with their corresponding clutter-free counterparts, make up the experimental dataset [41].

We calculate peak signal-to-noise ratio (PSNR) and the structural similarity index (SSIM) [19] for each test data. A high Peak Signal-to-Noise Ratio (PSNR) indicates that the predicted image closely resembles the reference image. The PSNR can be defined as,

$$PSNR(dB) = 10log\Big(\frac{1}{MSE(X,Y)}\Big) \tag{4.1}$$

$$MSE(X,Y) = \frac{1}{n}\sum_{i=1}^{n}\big(X_i - Y_i\big)^2 \tag{4.2}$$

In PSNR calculation, we first calculate the Mean Squared Error (MSE) using Equation (14), where n refers to the number of test data, X represents the reference image, and Y represents the sparse component obtained from the network. SSIM is used as a metric to measure the similarity between two given images and it is calculated as,

$$SSIM(X,Y) = \frac{(2\mu_x\mu_y + C_1)(2\sigma_x y + C_2)}{(\mu_x^2 + \mu_y^2 + C_1)(\sigma_x^2 + \sigma_y^2 + C_2)} \tag{4.3}$$

The SSIM outcomes vary from 0 to 1, with 1 indicating a flawless match between the reference image and the sparse component image.

In Figure 4.1, the performance of different models on the hybrid dataset is shown. In panel (a), raw GPR image is represented, while panel (b) shows reference GPR image. The SVD method removes most of the clutter, although some clutter can still be observed around the target that is depicted in panel (c). On the other hand in panel (d), the RPCA method effectively remove the clutter, resulting in a clear view of the target.

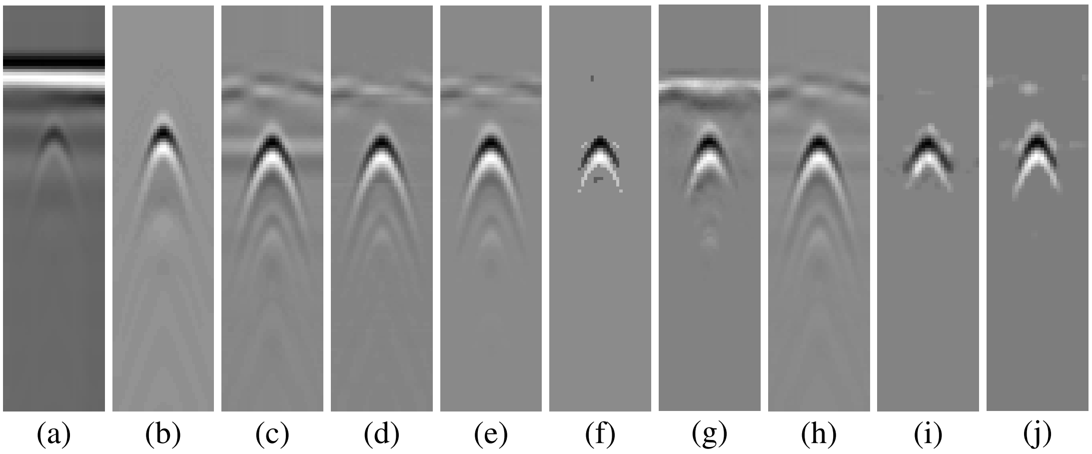

Figure 4.1 : Clutter removal methods for Image-1 (single target case) (a) raw image, (b) reference image, target images recovered by (c) SVD, (d) RPCA, (e) RNMF, (f) GoDec, (g) RAE, (h) LRPCA, (i) CORONA, (j) GODEC-Net.

However, some small residual clutters can remain, and the quality of the resulting image may have slightly decreased. In contrast, the RNMF method performs well in all conditions, making it the optimal choice compared to the other methods. RNMF result is shown in panel (e). It can be observed that GoDec removes the entirety of the clutter. However, it can be said that it slightly truncates a portion of the target in the image. The RAE method also performs well, but it may not be able to remove all of the clutter. In panel (g), the LRPCA method produces results similar to SVD, where the target is clearly visible, and most of the clutter is removed. The CORONA result is displayed in panel (i), demonstrating successful clutter removal similar to GoDec. However, it is evident that the target is truncated in the image. Our new method, GODEC-Net, yields superior results compared to CORONA in this particular case. Figure 4.2 illustrates the clutter removal outcome of the GPR image in the presence of multiple targets. The original B-Scan GPR image is displayed in Figure 4.2 (a), while the reference image is shown in Figure 4.2 (b). In this scenario, the targets are located near the surface. Although all methods exhibit visually similar results, there are subtle performance variations among them. SVD effectively removes clutter, as depicted in Figure 4.2 (c). RAE significantly eliminates most of the clutter, surpassing SVD in terms of performance. Similar to the previous figure, RNMF achieves the highest result based on the PSNR measurement. LRPCA appears as the second-best method, providing results closest to RNMF. CORONA and GODEC-Net successfully

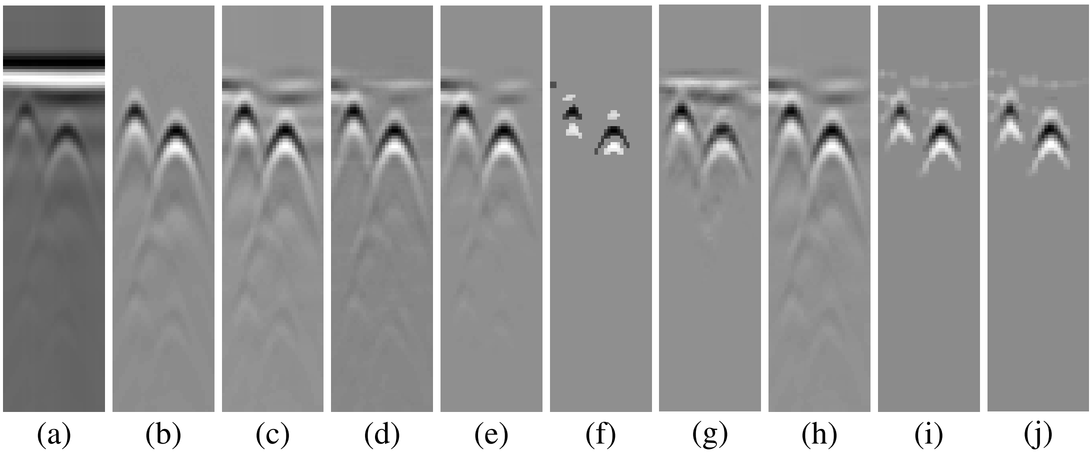
(a) (b) (c) (d) (e) (f) (g) (h) (i) (j)

Figure 4.2 : Clutter removal results for Image 2 (multiple target case): (a) raw image, (b) reference image, target images recovered by (c) SVD, (d) RPCA, (e) RNMF, (f) GoDec, (g) RAE, (h) LRPCA, (i) CORONA, (j) GODEC-Net.

remove the entire clutter, as seen in Figure 4.1. However, the issue of truncation affects the measurement performance.

Table 4.1 : Results of the Quantitative Metrics of Different Clutter Removal Methods For Single Target.

Methods	PSNR (dB)	SSIM
SVD	21.8177	0.8113
RPCA	21.8848	0.8531
RNMF	**22.7873**	0.8606
GoDec	21.5087	0.8628
RAE	22.4874	0.7591
LRPCA	22.6913	0.8468
CORONA	21.4941	**0.8817**
GODEC-Net	20.0875	0.8622

Table 4.1 presents a comparison of various methods used to remove clutter for a single target, and it shows that RNMF performs the best in terms of both PSNR. LRPCA appears to be the second-best method after RNMF in terms of producing satisfactory results. The results in the table confirm the visual outcomes. However, due to the

difference between PSNR and SSIM calculations, CORONA and GODEC-Net yield better results here compared to other methods.

Table 4.2 : Results of the Quantitative Metrics of Different Clutter Removal Methods For Multiple Targets.

Methods	**PSNR (dB)**	**SSIM**
SVD	28.6105	0.9358
RPCA	29.5923	0.9527
RNMF	**31.0758**	**0.9550**
GoDec	28.9122	0.9066
RAE	28.1836	0.8991
LRPCA	30.1207	0.9493
CORONA	26.7737	0.9180
GODEC-Net	30.8664	0.9277

Table 4.2 provides a comparison of clutter removal methods' performance for scenarios with multiple targets. The table indicates that RNMF exhibits the best performance for both metrics, consistent with the results presented in Table 4.1. LRPCA performs well, particularly in situations with multiple targets, outperforming RPCA. GODEC-Net delivers superior results compared to other methods, except for RNMF. Both traditional and proposed methods demonstrate successful clutter removal capabilities.

Our goal in this paper is to demonstrate not only the PSNR and SSIM performance of LRPCA, but also how much faster it is compared to other iterative algorithms. Therefore, the table below shows the processing time for 160 test images we have allocated for the hybrid dataset. In Table 4.3, it can be seen that LRPCA provides by far the fastest results. Except for RAE, other deep learning methods demonstrate faster performance during testing. As a result, this indicates that these methods can be used in real-world applications.

Table 4.3 : Average Run-Time of the Methods.

Methods	**Time (s)**
SVD	1.1564
RPCA	3.7539
RNMF	1.1235
GoDec	0.9878
RAE	7.5236
LRPCA	**0.6870**
CORONA	1.0123
GODEC-Net	0.9863

4.2 Real-GPR Dataset Results

The Real-GPR dataset is created using Geophysical Survey Systems Inc.(GSSI) SIR 4000 at TUBITAK Information Technologies Institute (TUBITAK BILGEM). The antenna is 400MHz (GSSI 50400S) whose dimensions are $30 \times 30 \times 17$ cm that is located 6 cm above the surface. The dataset contains two different types of buried targets that are teapots and metal discs. The teapot dimensions are $15 \times 15 \times 15$ cm, whereas the metal disc dimensions are $25 \times 25 \times 2$ cm also that are positioned at 20 cm and 30 cm below the surface, respectively. The targets were specifically chosen because the teapot is hard to detect by GPR antennas, while the metal disc is easier to detect because of its large surface area. The measurement setup is established using two types of soil pools whose dimensions are $3 \times 7 \times 4$ meters. Soil pool-1 includes the river type of soil, while soil pool-2 includes hard type of soil. The soil pools are kept dry at all times with special methods to avoid the effects of moisture. Moreover, the electromagnetic properties of soils are different from each other. The dataset were collected from soil pools using GSSI SIR 4000 the movement was +/- x directions. The simulated form of the experimental scenarios is shown in Figure 4.3.

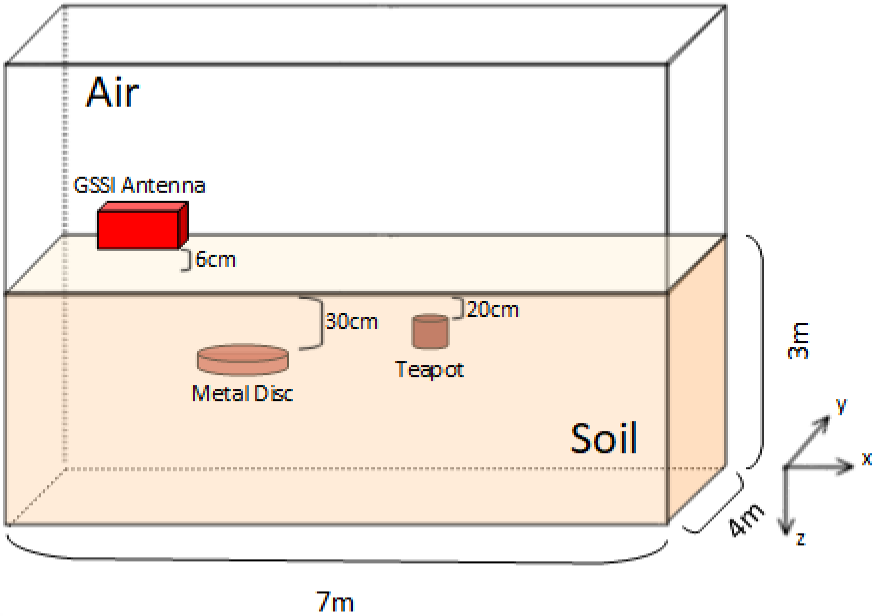

Figure 4.3 : Illustration of experimental scenarios.

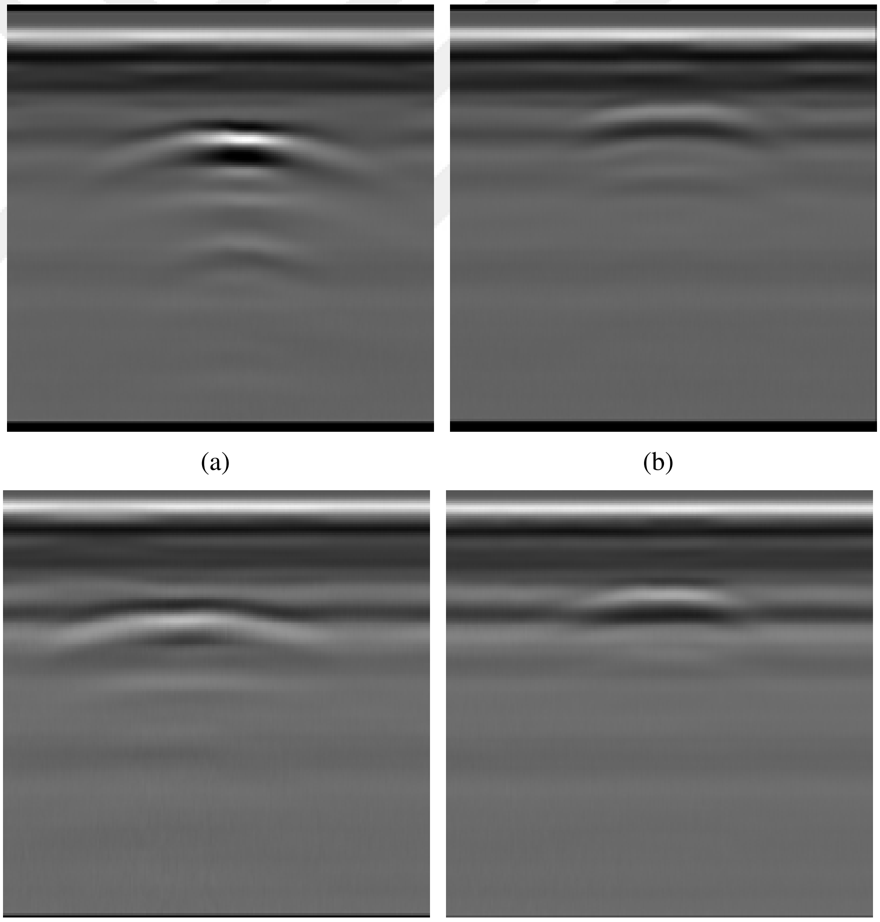
(a)
(b)
(c)
(d)

Figure 4.4 : Illustration of collected raw GPR imgaes. (a) metal disc and (b) teapot in soil type-1, (c) metal disc and (d) teapot in soil type-2.

The antennas always were in a fixed position because the movement was on a flat surface. The dataset consists of 1700 B-Scan images; 898 of them were target data and 802 of them were background data. All dataset is generated in two scenarios. In scenario-I, the targets are in soil pool-1 which is a river type of soil. Two targets are placed in the pool at 20 cm and 30 cm depths and the distance between each other is 40 cm. In this scenario, 1135 B-scan images are generated and 617 of them target others are background data. In scenario-II, the targets are positioned in soil pool-2 which is hard type soil. The target depths are the same in pool-1, but the electromagnetic properties of soil types are different. In scenario-II, 565 B-scan images are collected, 281 of them target data, and others are background data. Figure 4.5 displays our chosen targets, which include a teapot and a metal disc. We selected the teapot for its distinctive shape, but it is also noteworthy that it can be used as a handmade explosive. The metal disc is shown in Figure 4.5 (b). Additionally, Figures 4.5 (c) and (d) illustrate the soil pools.

The Real-GPR dataset comprises raw B-Scan images, which are depicted in Figure 4.3. Specifically, Figure 4.3 (a) displays a metal disc, and Figure 4.3 (b) shows a teapot, both of which are buried in soil type-1. Additionally, panels (c) and (d) of Figure 4.3 correspond to a metal disc and a teapot, respectively, that are located in soil type-2.

Figure 4.6 shows a comparison of model performances on the Real-GPR dataset. Unlike the hybrid dataset, there are no reference images available, making it impossible to conduct quantitative evaluations. Thus, only visual assessments are presented. Specifically, Figure 4.6 (a) displays raw images collected from soil type-1 and the target is metal disc. In Figure 4.6 (b), the SVD method has removed most of the clutter, but some clutter remains on top of the target's hyperbola. RPCA effectively removes almost all clutter, as shown in Figure 4.6 (c). Furthermore, RNMF outperforms all other methods, just like in the hybrid dataset. GoDec's clutter removal performance is almost the same as SVD, as depicted in Figure 4.6 (e). The RAE decomposes the target and clutter, as shown in Figure 4.6 (f). However, when compared to other methods, there is a larger amount of clutter present. LRPCA, similar to RPCA, has effectively removed most of the noise, and the target is clearly visible in Figure 4.6 (g) .Figures

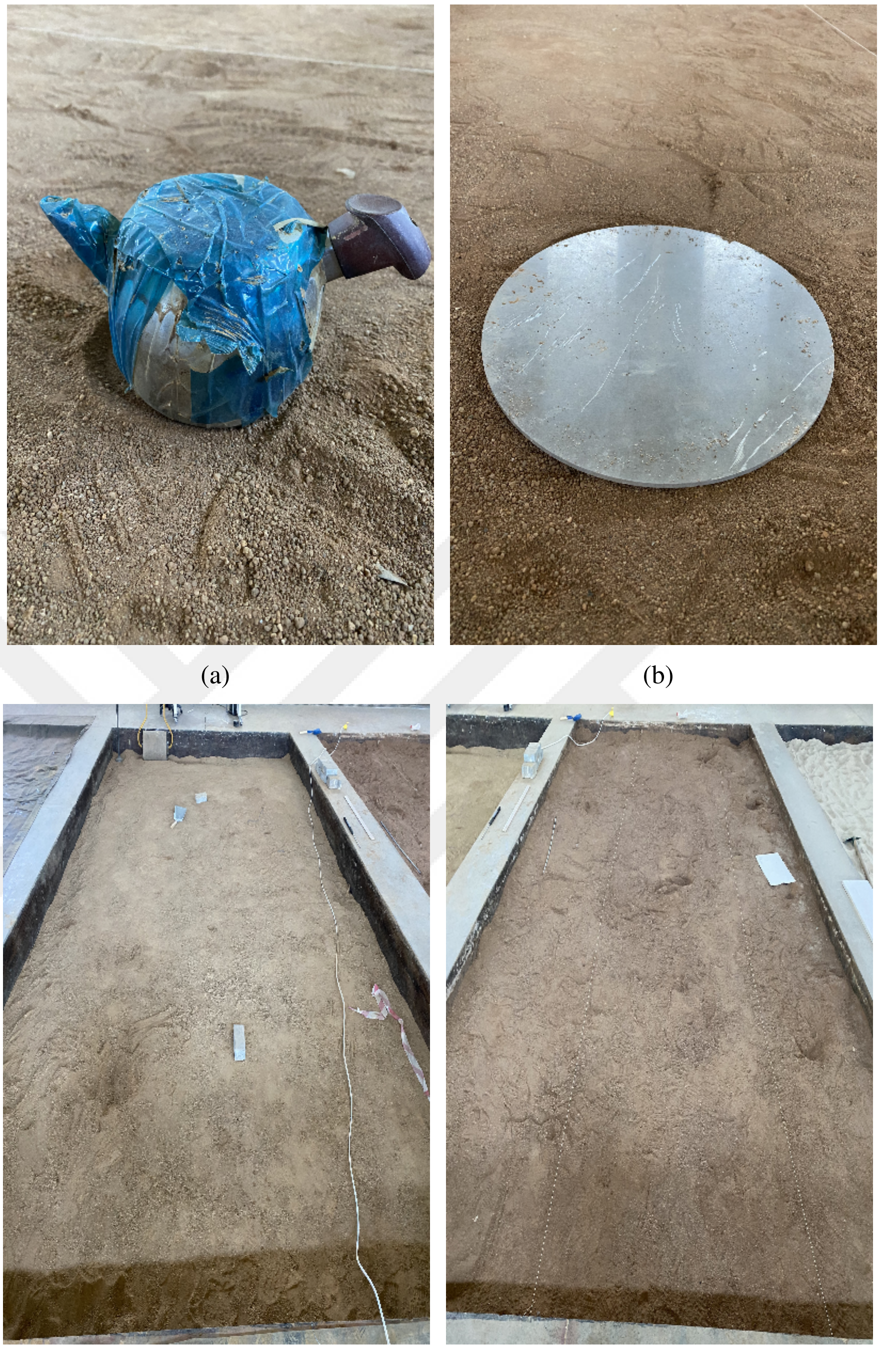

(a) (b)

(c) (d)

Figure 4.5 : Demonstration of measurement environment and target that is used to create Real-GPR dataset. (a) A teapot filled with sand inside has been selected as a target. It is preferred due to its similarity to handmade explosives. (b) shows the metal disc, which is the other target. (c)-(d) show the soil pools that we named soil type-1 and soil type-2, respectively.

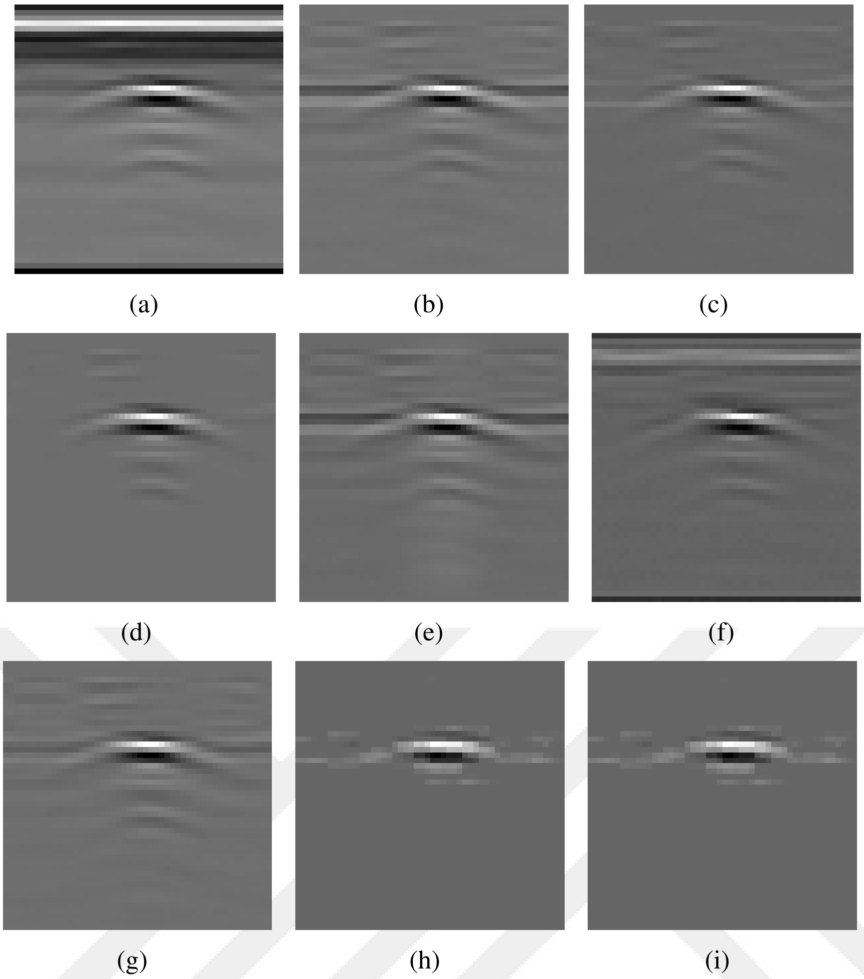

(a) (b) (c)

(d) (e) (f)

(g) (h) (i)

Figure 4.6 : Illustration of the experimental results, (a) raw image, (b) SVD, (c) RPCA, (d) RNMF, (e) GoDec, (f) RAE, (g) LRPCA, (h) CORONA, (i) GODEC-Net.

4.6 (h) and 4.6 (i) show the performance of CORONA and GODEC-Net, respectively. Both methods yield similar visual results, but due to the CORONA architecture, there is some loss of detail around the target.

Figure 4.7 showcases the outcomes of clutter removal for a teapot buried in soil type-1. The results obtained from all methods demonstrate successful clutter removal, resulting in clean outputs. Specifically, Figures 4.7 (b) and (e) display the performance of the SVD and GoDec methods, respectively. Both methods exhibit similar results with some residual clutter surrounding the target. In contrast, Figures 4.7 (c) and (d) present the outcomes achieved by the RPCA and RNMF methods, respectively. Among them, RNMF produces the best outcome, while LRPCA also performs well with some remaining clutter. In Figure 4.7 (f), the results of RAE are shown. It can

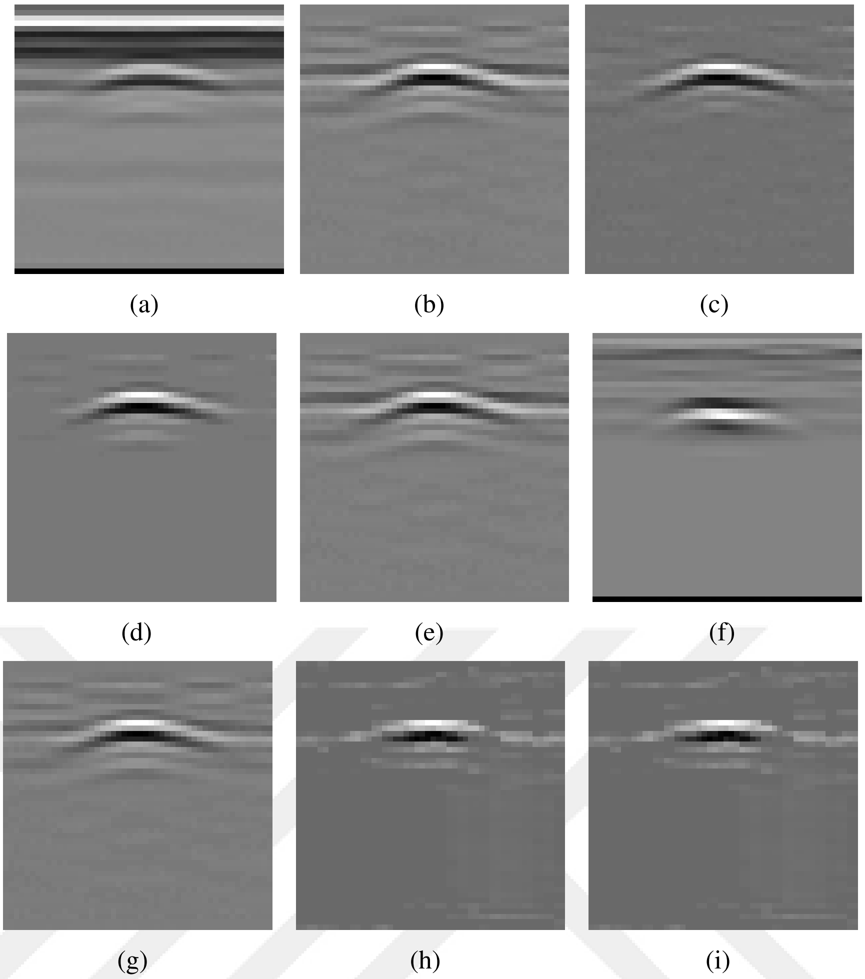
(a) (b) (c)

(d) (e) (f)

(g) (h) (i)

Figure 4.7 : Illustration of the experimental results, (a) raw image, (b) SVD, (c) RPCA, (d) RNMF, (e) GoDec, (f) RAE, (g) LRPCA, (h) CORONA, (i) GODEC-Net.

be observed that RAE effectively removes most of the clutter, but it performs worse compared to other methods in these scenarios. The clutter removal performances of CORONA and GODEC-Net are depicted in Figures 4.7 (h) and (i), respectively. It is evident that the unrolled methods can be effectively utilized for clutter removal in GPR images. Compared to Figure 4.6, the results in Figure 4.7 appear slightly noisier due to the teapot's proximity to the surface.

Figure 4.8 showcases the clutter removal results for GPR images captured from soil type-2, which includes a metal disc. The method's performance shows a slight compromise when compared to that of soil type-1. This is due to the harder nature of soil type-2, which impacts the results, as illustrated in Figure 4.8. Among the evaluated models, RNMF demonstrates the best performance. While RPCA performs

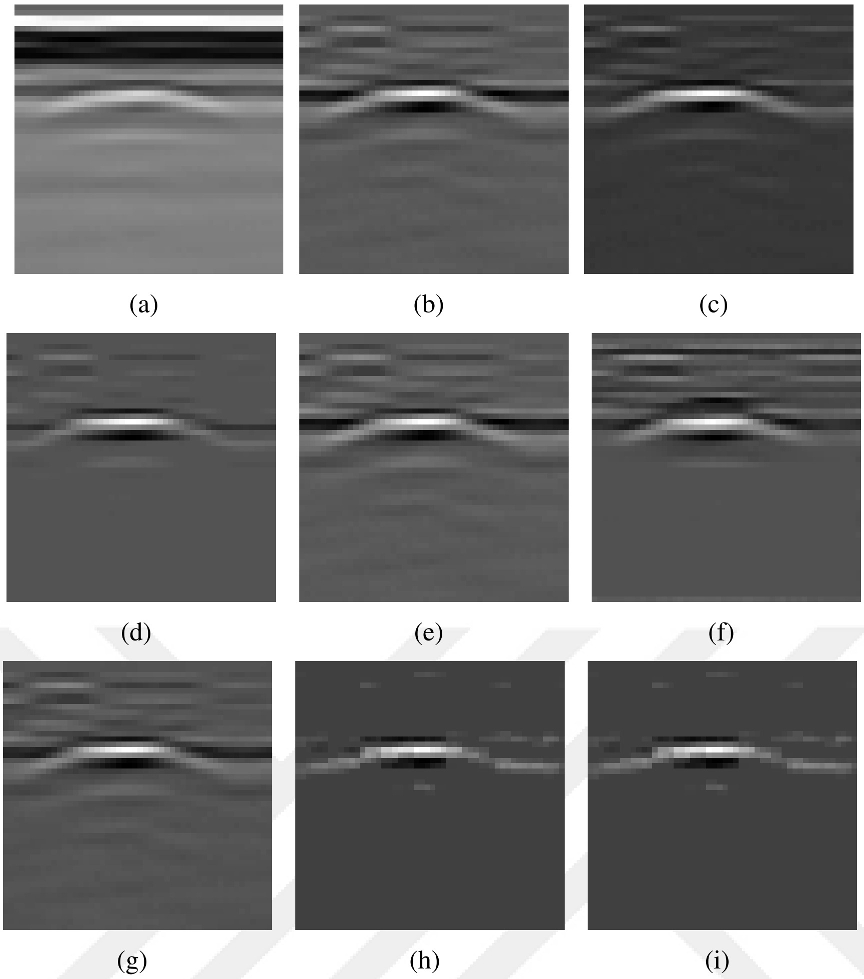

(a) (b) (c)
(d) (e) (f)
(g) (h) (i)

Figure 4.8 : Illustration of the experimental results, (a) raw image, (b) SVD, (c) RPCA, (d) RNMF, (e) GoDec, (f) RAE, (g) LRPCA, (h) CORONA, (i) GODEC-Net.

similarly to RNMF, some residual clutter remains at the end of the hyperbola of the targets. GoDec successfully removes a significant portion of the clutter, making the target clearly visible, but some remaining clutter appears horizontally at the target's position. In Figure 4.8 (g), LRPCA's result separates the target from the raw image, but some clutter remains due to the influence of the soil type. As for CORONA, it effectively removes the clutter from the raw GPR images, but it also eliminates a small portion of the target from the images. GODEC-Net follows a similar pattern to the original CORONA algorithm. Figure 4.9 showcases the clutter removal results for a teapot buried in soil type-2. In panel (a), the raw GPR images are presented, while panel (b) demonstrates the clutter removal performance of the conventional method SVD, which successfully extracts the target in this scenario. Panel (c) illustrates the result of RPCA, which effectively decomposes the target and the clutter. Once again,

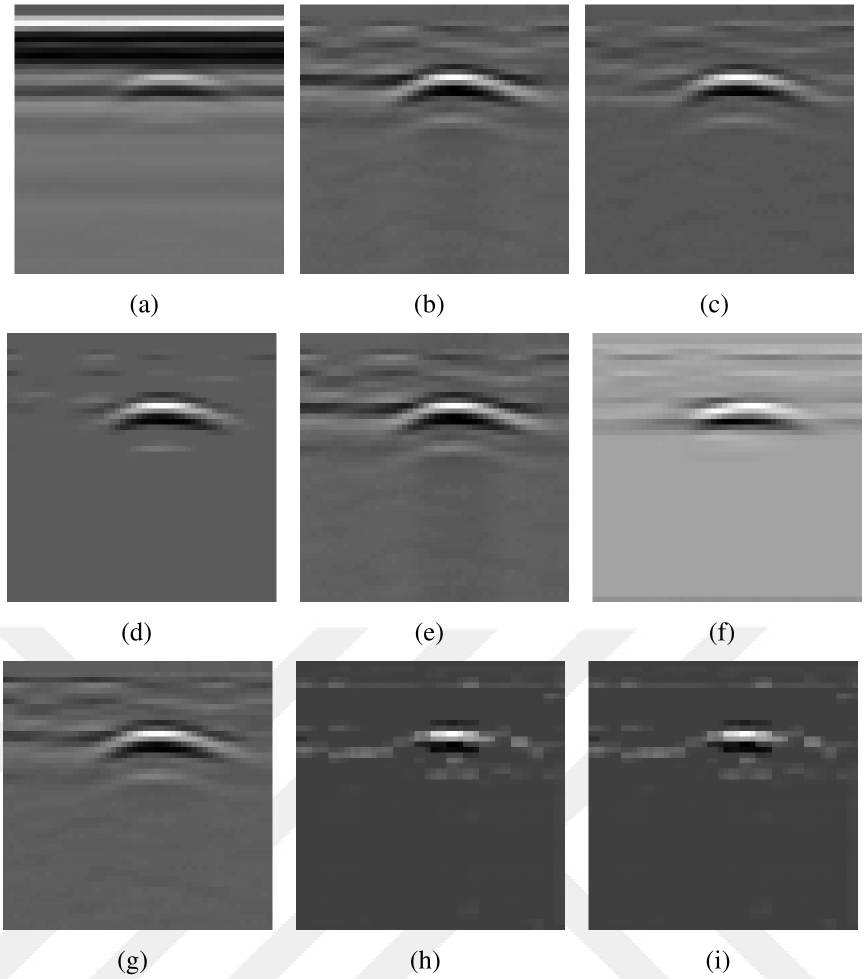

(a) (b) (c)

(d) (e) (f)

(g) (h) (i)

Figure 4.9 : Illustration of the experimental results, (a) raw image, (b) SVD, (c) RPCA, (d) RNMF, (e) GoDec, (f) RAE, (g) LRPCA, (h) CORONA, (i) GODEC-Net.

RNMF yields the best result across all scenarios, with a clear background and a clearly visible target. In Figure 4.9 (e), it demonstrates how GoDec separates the target from the raw data. As seen, there is still some clutter present. RAE separates the raw image into the target and clutter, as shown in Figure 4.9 (f), but some clutter still remains around the target. LRPCA, similar to other methods, shows very good performance. Other Unfolded methods, such as LRPCA, are shown in Figure (h) and (i), and they have also successfully removed most of the clutter. However, the only drawback is that the target appears slightly truncated.

4.3 Training the Dataset

The unfolded methods were trained using Python 3.8.16 and PyTorch 1.7.1, utilizing both the hybrid dataset and the Real-GPR dataset. The training was performed on an Nvidia GTX 1060Ti graphics card with 16 GB of DDR4 RAM.

Due to memory constraints when training the hybrid dataset, a batch size of 1 was chosen, and the original images were resized to dimensions of 128×32 pixels. CORONA and GODEC-Net were trained with 10 layers. The first three layers employed convolution filters of size $5 \times 5 \times 1$ with a stride of (1, 1, 1), padding of $(2,2,0)$, and a bias term. The remaining seven layers used filters of size $3 \times 3 \times 1$ with a stride of $(1,1,1)$, padding of $(1,1,0)$, and a bias term.

The ADAM optimizer [44] is utilized with default parameters, and the initial learning rate was set to 0.002 for network optimization. For the hybrid dataset, a total of 2400 images were selected, with 2000 images allocated for training and 400 images for validation. Additionally, 500 GPR images were chosen for testing the hybrid dataset. Regarding LRPCA, 10 layers were selected, similar to the other unfolded networks, and the learning rates were set to 0.001.

The Real-GPR dataset consists of 617 GPR images that were used to train the proposed methods. Out of these images, 517 were allocated for training purposes, and 100 were set aside for validation. Furthermore, a total of 281 images were utilized to evaluate and assess the performance of the models.

The L and S components, which are essential for calculating losses at each step, were obtained using traditional RPCA. In the RPCA process, a lambda value of 0.08 was selected. For RNMF, the lambda value was set to 0.05. Furthermore, a trained RAE was employed, utilizing a learning rate of 0.003 and a batch size of 20.

Table 4.4 provides a comparison of the average execution time per batch for both the CORONA algorithm and our proposed method. In one batch, our model took approximately 365.14 seconds to run during the training phase and 24.10 seconds during the validation phase. The CORONA algorithm took around 5 hours and 40

Table 4.4 : Average Run-Time of Batches.

Methods	Training-Time (s)	Validation-Time (s)
CORONA	365.1416	24.1031
GODEC-Net	**239.2298**	**9.6448**

minutes to run in total. On the other hand, our proposed algorithm took only 239.22 seconds during the training phase and 9.64 seconds during the validation phase in one batch. In total, it took approximately 3 hours 40 minutes to complete. These results indicate that our method is approximately 56.40% faster than the original CORONA algorithm.

Table 4.5 : Average Run-Time of Batches.

Methods	Training-Time (s)	Validation-Time (s)
CORONA	72.9818	5.7319
GODEC-Net	**57.3304**	**3.3667**

A comparison between the average time taken by the CORONA algorithm and our proposed method for each batch is presented by Table 4.5. In one batch, our model took approximately 72.98 seconds for the training phase and 5.73 seconds for the validation phase, while the CORONA algorithm took around 1 hours and 10 minutes to complete. On the other hand, our proposed algorithm took only 57.33 seconds for the training phase and 3.36 seconds for the validation phase in one batch, and it took approximately 45 minutes to complete in total. Based on these results, it can be concluded that our method is approximately 30% faster than the original CORONA algorithm.

5. CONCLUSIONS

In this thesis, three different deep unfolded networks are proposed: Learned Robust Principal Component Analysis (LRPCA), Convolutional Robust Principal Component Analysis, and Go-Decomposition Network (GODEC-Net). These proposed methods are designed for clutter removal from GPR images, offering an alternative to traditional approaches. The utilization of deep unfolded networks brings key advantages such as reduced computational costs and faster execution time. By employing these methods, the efficiency and effectiveness of clutter removal can be greatly enhanced.

The numerical results are derived through calculations of peak signal-to-noise ratio (PSNR) and structural similarity index (SSIM). A higher PSNR value signifies a close resemblance between the predicted image and the reference image. The SSIM results range from 0 to 1, with a value of 1 indicating a perfect match between the reference image and the sparse component image.

LRPCA employs a novel FRMNN model that extends deep unfolding from finite iterations to infinite iterations, resulting in reduced runtime during the test phase when compared to traditional methods. This approach also enables the learnability of hyperparameters. To evaluate LRPCA, it was tested on both a hybrid dataset and a newly generated real dataset. The visual outcomes of LRPCA, in terms of clutter removal from GPR images, surpass those of RAE, GoDec, RPCA, and SVD. LRPCA effectively removes a significant portion of clutter, as confirmed by both the visual results and the numerical computations, thus demonstrating a high level of accuracy. Furthermore, LRPCA showcases faster separation of GPR images during the test phase compared to traditional methods.

CORONA utilizes convolutional kernels instead of fully connected layers, enabling the model to achieve spatial invariance while significantly reducing the number of parameters that need to be learned. Although initially designed for tissue/contrast separation in ultrasound images, CORONA has been successfully applied to effectively separate target and clutter in GPR images. The results clearly indicate that most of the clutter has been successfully removed from GPR images in both datasets. CORONA outperforms various traditional methods in clutter removal, as evidenced by the improved visual outcomes. Additionally, CORONA demonstrates superior numerical results, particularly in the SSIM calculation, when compared to other methods.

GODEC-Net can be considered an accelerated version of CORONA as it employs BRP instead of SVD when separating the clutter component. GODEC-Net produces results that are comparable to CORONA in both numerical and visual aspects. When comparing the proposed methods, they consistently demonstrate superior performance both visually and numerically in various scenarios. The novel GODEC-Net model exhibits higher numerical performance, particularly in scenarios with multiple targets present in the hybrid dataset, outperforming SVD, RPCA, GoDec, RAE, and even CORONA in terms of the PSNR metric.

It is mentioned that the purpose of using unfolded deep network methods is to reduce the high computational cost and long processing times associated with traditional iterative methods. To evaluate this, 160 GPR images are tested. While GPR images are solved iteratively by iterative algorithms, the proposed methods separate the GPR images into target and sparse components using learned coefficients and parameters during training. The conducted tests show that LRPCA provides faster results compared to both unfolded methods and other clutter removal techniques. However, when CORONA and GODEC-Net are compared with each other during the testing phase, it is noted that GODEC-Net yields slightly faster results. Finally, a comparison is made between the training times of CORONA and GODEC-Net. The reason for specifically comparing these two methods is to demonstrate how the algorithm speeds up when using BRP instead of SVD in our proposed new method.

As future work for this thesis, the LRPCA can be further accelerated by leveraging tensor RPCA (TRPCA) [45] techniques. On the other hand, enhancing the outcomes further can be achieved by expanding the dataset with more scenarios, even though the proposed methods already deliver good visual results.

REFERENCES

[1] **Francke, J.** (2012). A review of selected ground penetrating radar applications to mineral resource evaluations, *Journal of Applied Geophysics*, *81*, 29–37, `https://www.sciencedirect.com/science/article/pii/S0926985111002126`, recent, Relevant and Advanced GPR Studies in Applied Geophysics.

[2] **Conyers, L.B.** (2011). Discovery, mapping and interpretation of buried cultural resources non-invasively with ground-penetrating radar, *Journal of Geophysics and Engineering*, *8*(3), S13–S22, `https://doi.org/10.1088/1742-2132/8/3/S02`, `https://academic.oup.com/jge/article-pdf/8/3/S13/26801308/jge11\_3\_s02.pdf`.

[3] **Lombardi, F.**, **Lualdi, M.**, **Picetti, F.**, **Bestagini, P.**, **Janszen, G. and Di Landro, L.A.** (2020). Ballistic Ground Penetrating Radar Equipment for Blast-Exposed Security Applications, *Remote Sensing*, *12*(4), `https://www.mdpi.com/2072-4292/12/4/717`.

[4] **Daniels, D.J.** Ground Penetrating Radar, John Wiley Sons, Ltd.

[5] **Jol, H.M.** (2009). Errata, Elsevier, Amsterdam, pp.1–2.

[6] **Solimene, R.**, **Cuccaro, A.**, **Dell'Aversano, A.**, **Catapano, I. and Soldovieri, F.** (2014). Ground Clutter Removal in GPR Surveys, *IEEE Journal of Selected Topics in Applied Earth Observations and Remote Sensing*, *7*(3), 792–798.

[7] **Kumlu, D. and Erer, I.** (2019). Clutter removal techniques in ground penetrating radar for landmine detection: A survey, *Operations Research for Military Organizations*.

[8] **Singh, P.K.V.A.N.G.D. and Nigam, M.J.** (2009). Analysis of Clutter Reduction Techniques for through Wall Imaging in UWB Range, *Progress In Electromagnetics Research B*, *17*, 29–48.

[9] **Kumlu, D. and Isin Erer, I.** (2018). Clutter removal in GPR images using non-negative matrix factorization, *Journal of Electromagnetic Waves and Applications*, *32*(16), 2055–2066.

[10] **Zhou, T. and Tao, D.** (2012). Bilateral random projections, *2012 IEEE International Symposium on Information Theory Proceedings*, pp.1286–1290.

[11] **Kumlu, D. and Erer, I.** (2020). Improved Clutter Removal in GPR by Robust Nonnegative Matrix Factorization, *IEEE Geoscience and Remote Sensing Letters*, *17*(6), 958–962.

[12] **Ni, Z.K.**, **Ye, S.**, **Shi, C.**, **Li, C. and Fang, G.** (2022). Clutter Suppression in GPR B-Scan Images Using Robust Autoencoder, *IEEE Geoscience and Remote Sensing Letters*, *19*, 1–5.

[13] **Monga, V.**, **Li, Y. and Eldar, Y.C.** (2021). Algorithm Unrolling: Interpretable, Efficient Deep Learning for Signal and Image Processing, *IEEE Signal Processing Magazine*, *38*(2), 18–44.

[14] **Temlioglu, E. and Erer, I.** (2022). A Novel Convolutional Autoencoder-Based Clutter Removal Method for Buried Threat Detection in Ground-Penetrating Radar, *IEEE Transactions on Geoscience and Remote Sensing*, *60*, 1–13.

[15] **Bouwmans, T.**, **Javed, S.**, **Zhang, H.**, **Lin, Z. and Otazo, R.** (2018). On the Applications of Robust PCA in Image and Video Processing, *Proceedings of the IEEE*, *106*(8), 1427–1457.

[16] **Schwartz, C.**, **Ramos, L.P.**, **Duarte, L.T.**, **Pinho, M.d.S.**, **Pettersson, M.I.**, **Vu, V.T. and Machado, R.** (2020). Change Detection in UWB SAR Images Based on Robust Principal Component Analysis, *Remote Sensing*, *12*(12), `https://www.mdpi.com/2072-4292/12/12/1916`.

[17] **Song, X.**, **Xiang, D.**, **Zhou, K. and Su, Y.** (2017). Improving RPCA-Based Clutter Suppression in GPR Detection of Antipersonnel Mines, *IEEE Geoscience and Remote Sensing Letters*, *14*(8), 1338–1342.

[18] **Zhou, T. and Tao, D.** (2011). GoDec: Randomized Low-Rank Sparse Matrix Decomposition in Noisy Case, 33–40.

[19] **Luo, T.X.H.**, **Lai, W.W.L. and Lei, Z.** (2023). Intensity Normalisation of GPR C-Scans, *Remote Sensing*, *15*(5), `https://www.mdpi.com/2072-4292/15/5/1309`.

[20] **Malof, J.M.**, **Reichman, D.**, **Karem, A.**, **Frigui, H.**, **Ho, K.C.**, **Wilson, J.N.**, **Lee, W.H.**, **Cummings, W.J. and Collins, L.M.** (2019). A Large-Scale Multi-Institutional Evaluation of Advanced Discrimination Algorithms for Buried Threat Detection in Ground Penetrating Radar, *IEEE Transactions on Geoscience and Remote Sensing*, *57*(9), 6929–6945.

[21] **Ozkaya, U.**, **Melgani, F.**, **Belete Bejiga, M.**, **Seyfi, L. and Donelli, M.** (2020). GPR B scan image analysis with deep learning methods, *Measurement*, *165*, 107770, `https://www.sciencedirect.com/science/article/pii/S0263224120303080`.

[22] **Bestagini, P.**, **Lombardi, F.**, **Lualdi, M.**, **Picetti, F. and Tubaro, S.** (2021). Landmine Detection Using Autoencoders on Multipolarization GPR

Volumetric Data, *IEEE Transactions on Geoscience and Remote Sensing*, *59*(1), 182–195.

[23] **Hou, B.**, **Kou, H. and Jiao, L.** (2016). Classification of Polarimetric SAR Images Using Multilayer Autoencoders and Superpixels, *IEEE Journal of Selected Topics in Applied Earth Observations and Remote Sensing*, *9*(7), 3072–3081.

[24] **Candès, E.J.**, **Li, X.**, **Ma, Y. and Wright, J.** (2011). Robust Principal Component Analysis?, *J. ACM*, *58*(3), `https://doi.org/10.1145/1970392.1970395`.

[25] **Cai, H.**, **Liu, J. and Yin, W.** (2021). *Learned Robust PCA: A Scalable Deep Unfolding Approach for High-Dimensional Outlier Detection*, `2110.05649`.

[26] **Solomon, O.**, **Cohen, R.**, **Zhang, Y.**, **Yang, Y.**, **He, Q.**, **Luo, J.**, **van Sloun, R.J.G. and Eldar, Y.C.** (2020). Deep Unfolded Robust PCA With Application to Clutter Suppression in Ultrasound, *IEEE Transactions on Medical Imaging*, *39*(4), 1051–1063.

[27] **Yu, S.H.**, **Mehra, R.K. and Witten, T.R.** (1999). Automatic mine detection based on ground-penetrating radar, ***A.C. Dubey***, ***J.F. Harvey***, ***J.T. Broach and R.E. Dugan****, editors, Detection and Remediation Technologies for Mines and Minelike Targets IV*, volume3710, International Society for Optics and Photonics, SPIE, pp.961 – 972, `https://doi.org/10.1117/12.357116`.

[28] **Mellett, J.S.** (1995). Ground penetrating radar applications in engineering, environmental management, and geology, *Journal of Applied Geophysics*, *33*(1), 157–166, `https://www.sciencedirect.com/science/article/pii/0926985195900381`.

[29] **Limp, W.** (2006). Ground Penetrating Radar for Archaeology by Lawrence B. Conyers, *Journal of Field Archaeology*, *31*, 105–107.

[30] **Manenti, R.**, **Ufba, C. and Williams, K.** (2015). Using Ground Penetrating Radar to Locate Historical Graves in Western New York.

[31] **Kovin, O.** (2010). Fractures imaging in the Upper Kama potash mine using 3-D GPR data, volume 2.

[32] **Daniels, D.** (2006). A review of GPR for landmine detection, *Sensing and Imaging*, *7*, 90–123.

[33] **Sadek, R.A.** (2012). *SVD Based Image Processing Applications: State of The Art, Contributions and Research Challenges*, `1211.7102`.

[34] **Workalemahu, T.** (2008). Singular Value Decomposition in Image Noise Filtering and Reconstruction.

[35] **Abujarad, F. and Omar, A.** (2006). GPR Data Processing Using the Component-Separation Methods PCA and ICA, *Proceedings of the 2006 IEEE International Workshop on Imagining Systems and Techniques (IST 2006)*, pp.60–64.

[36] **Recht, B.** (2009). *A Simpler Approach to Matrix Completion*, `0910.0651`.

[37] **Ke, Q. and Kanade, T.** (2005). Robust L/sub 1/ norm factorization in the presence of outliers and missing data by alternative convex programming, *2005 IEEE Computer Society Conference on Computer Vision and Pattern Recognition (CVPR'05)*, volume 1, pp.739–746 vol. 1.

[38] **Zhang, L.**, **Chen, Z.**, **Zheng, M. and He, X.** (2011). Robust non-negative matrix factorization, *Frontiers of Electrical and Electronic Engineering in China*, *6*, 192–200.

[39] **Gregor, K. and LeCun, Y.** (2010). Learning Fast Approximations of Sparse Coding, *International Conference on Machine Learning*.

[40] **Tong, T.**, **Ma, C. and Chi, Y.** (2021). *Accelerating Ill-Conditioned Low-Rank Matrix Estimation via Scaled Gradient Descent*, `2005.08898`.

[41] **Sun, H.H.**, **Cheng, W. and Fan, Z.** (2022). Learning to Remove Clutter in Real-World GPR Images Using Hybrid Data, *IEEE Transactions on Geoscience and Remote Sensing*, *60*, 1–14.

[42] **Warren, C.**, **Giannopoulos, A. and Giannakis, I.** (2016). gprMax: Open source software to simulate electromagnetic wave propagation for Ground Penetrating Radar, *Computer Physics Communications*, *209*, 163–170, `https://www.sciencedirect.com/science/article/pii/S0010465516302533`.

[43] **Warren, C.**, **Giannopoulos, A.**, **Gray, A.**, **Giannakis, I.**, **Patterson, A.**, **Wetter, L. and Hamrah, A.** (2019). A CUDA-based GPU engine for gprMax: Open source FDTD electromagnetic simulation software, *Computer Physics Communications*, *237*, 208–218, `https://www.sciencedirect.com/science/article/pii/S0010465518303990`.

[44] **Kingma, D.P. and Ba, J.** (2017). *Adam: A Method for Stochastic Optimization*, `1412.6980`.

[45] **Cai, H.**, **Chao, Z.**, **Huang, L. and Needell, D.** (2021). *Fast Robust Tensor Principal Component Analysis via Fiber CUR Decomposition*, `2108.10448`.

CURRICULUM VITAE

Samet ÖZGÜL

EDUCATION:

- **B.Sc.:** 2017, Balikesir University, Faculty of Engineering, Department of Electrical and Electronic Engineering

PROFESSIONAL EXPERIENCE AND REWARDS:

- 2018-2020 İstanbul Technical University at Aerospace Research Center
- 2020-... TUBITAK BILGEM

PUBLICATIONS, PRESENTATIONS AND PATENTS ON THE THESIS:

- **Özgül S., Erer I.**, An experimental study on low rank and sparse decomposition based approaches for clutter removal in GPR images., *2nd International Grauate Research Symposium*, May 16-18, 2023 Istanbul, Turkey.